JOHANNES GUTENBERG
UNIVERSITÄT MAINZ

EXPERIMENTE ZUR SUCHE NACH DUNKLEN PHOTONEN AM MAINZER MIKROTRON

Harald Merkel

Habilitationsschrift

zur Erlangung der *venia legendi*
im Fach „Experimentelle Physik“

vorgelegt beim
Fachbereich Physik, Mathematik und Informatik
der Johannes Gutenberg-Universität Mainz

November 2014

Inhalt

Zusammenfassung (Deutsch)

Das Rätsel der dunklen Materie ist eines der prominentesten Beispiele für Phänomene, die im Rahmen des Standardmodells der Teilchenphysik nicht erklärt werden können. Eine Reihe von Modellen zur Erweiterung des Standardmodells werden zur Zeit diskutiert, allerdings ist es bis jetzt nicht gelungen, ein experimentelles Signal der dunklen Materie jenseits der offensichtlichen Graviationswirkung nachzuweisen.

Aufgrund des überwältigenden Erfolges der Quantenfeldtheorien im Standardmodell liegt den meisten Modellen jenseits dessen eine Erweiterung der fundamentalen Symmetrien zugrunde, die in der Folge z.B. durch Methoden der Symmetriebrechung auf das beobachtbare Spektrum des Standardmodells heruntergebrochen werden müssen. Diese Modelle sagen daher in der Regel nicht nur ein einziges, isoliertes Teilchen der dunkeln Materie vorher, sondern einen reichhaltigen „dunklen Sektor“ der Teilchenphysik. Ein naheliegender Ansatz ist es, nach der einfachst möglichen Eichsymmetrie in diesem Sektor, einer $U(1)$ Symmetrie, zu suchen. Das Eichboson dieser Symmetrie hat eine nicht verschwindende Masse und die Quantenzahlen des Photons und wird häufig als „dunkles Photon“ γ' bezeichnet.

Im einfachsten Modell koppelt das dunkle Photon über den Mechanismus der kinetischen Mischung an die Materie des Standardmodells. Dieser kann über eine effektive Wechselwirkung $\epsilon e A'_\mu J^\mu_{EM}$ des dunklen Photon Feldes A' mit dem elektromagnetischen Strom J beschrieben werden. Hierbei beschreibt der Mischungsparameter $\epsilon^2 = \alpha'/\alpha$ die Stärke der Wechselwirkung.

Neben der starken theoretischen Motivation für eine dunkles Photon existieren aber auch einige bisher ungeklärte experimentelle Phänomene, die man auf eine mögliches dunkles Photon zurückführen kann. Unter anderem der beobachtete Überschuss an Positronen in der Galaxie kann von der Annihilation dunkler Materie über dunkle Photonen herrühren. Zwar gibt es hierfür auch konkurierende Erklärungsversuche, z.B. Positronenquellen wie Quasare, die Hypothese der dunklen Photonen kann allerdings das beobachtete Positronenspektrum sehr gut beschreiben.

Auch die Diskrepanz zwischen der Messung des anomalen magnetischen Moments des Muons $(g-2)_\mu$ und den Rechungen in QED kann auf natürliche Weise erklärt werden, wenn man einen Beitrag von dunklen Photonen in den Vertexkorrekturen mit berücksichtigt.

Die Gesamtheit der experimentellen Hinweise deutet auf einen Parameterbereich in der Masse des dunklen Photons von wenigen MeV bis ca. $1\,\mathrm{GeV}/c^2$ hin, sowie einen Bereich im Mischungsparameter von $10^{-12} < \epsilon < 10^{-3}$. Dieser Bereich liegt im Energiebereich des Mainzer Mikrotrons (MAMI).

In dieser Arbeit wurde eine experimentelles Programm zur Suche nach dunklen Photonen im Rahmen der A1-Kollaboration am Mainzer Mikrotron (MAMI) entwickelt. In einem ersten Pilotexperiment wurde gezeigt, dass die Kollaboration existierende Grenzen um fast eine Größenordnung in der Sensitivität übertreffen kann.

Für die Extraktion von Ausschlussgrenzen aus den experimentellen Daten ist die möglichst exakte Berechnung des erwarteten Signals sowie des elektromagnetischen Untergrundes durch Paarerzeugung essentiell. In einem theoretischen Papier wurden hierzu die Werkzeuge entwickelt und die Sensitivität weiterer Experimente, u.a. am sich im Aufbau befindenden Mainzer Beschleuniger MESA, untersucht.

In einem weiteren Experiment wurde eine Ausschlußgrenze bestimmt, die insbesondere den Bereich, in dem die Diskrepanz des anamalen magnetischen Moments des Muons durch ein dunkles Photon erklärt werden könnte, weitgehend abdeckt.

1 Introduction

1.1 Evidence for Dark Matter and a Dark Sector

Already in 1937 the Swiss astronomer F. Zwicky discovered, that the orbital motion of the COMA galaxy cluster does not show the expected radial behavior [1]. Assuming, that the centrifugal forces are equal to the gravitational forces, one expects via

$$\frac{v^2(r)}{r} = \frac{GM(r)}{r^2} \qquad \Rightarrow \qquad v(r) = \sqrt{\frac{GM(r)}{r}}$$

a velocity dependence which falls off with one over the square root of the radius. Instead, a nearly flat velocity distribution was observed. Zwicky concluded that unobserved matter, which he called “Dark Matter”, has to be present for an additional gravitational field.

Later, the same observation was made for galaxies and was confirmed for all objects on galactic scales where rotational curves could be extracted. Fig. 1 shows as an example the rotational curve of the galaxy M33 [2] and the visible contributions from the galactic disk and interstellar gas. Obvious, one needs to add an considerable halo of dark matter to explain the rotational curve within the standard gravitational law.

While the term “Dark Matter” was interpreted in the early years just as ordinary “matter we don’t see (yet)” and various possible conventional candidates were discussed in the literature, like isolated black holes, brown dwarfs, neutron stars etc., all proposed candidates are meanwhile excluded by careful astronomical observations, *e.g.* by searches for gravitational microlensing effects of such isolated but dense objects.

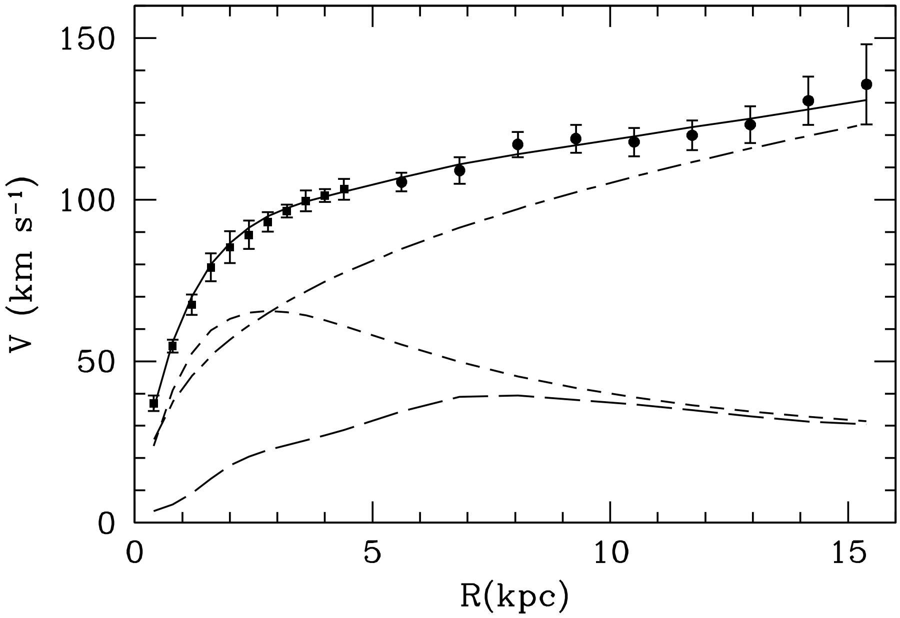

Figure 1: Rotation curve of the galaxy M33 (data points) compared with a fit of a dark matter model (solid line). Also shown are the contributions of the halo (dash-dotted line), the stellar disc (short-dashed line) and the interstellar gas (long-dashed line) [2].

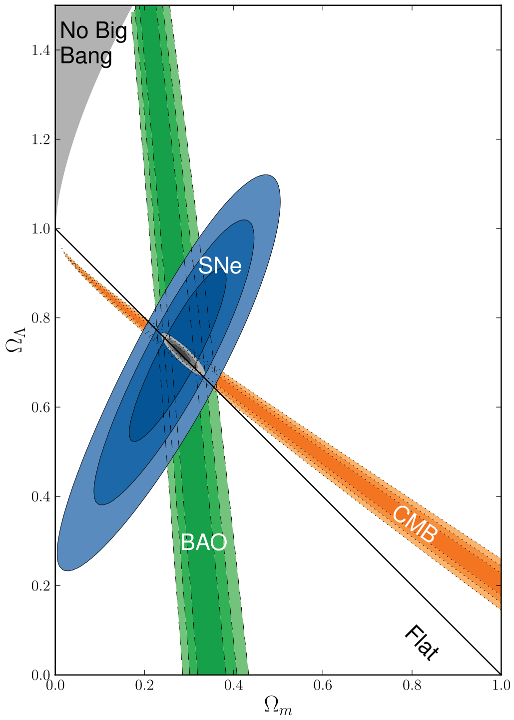

Figure 2: Fit of the mass density in the universe Ω_m and the dark energy content Ω_Λ to observations of supernova explosions (SNe), Baryonic Acoustic Oscillations (BAO) and multipole analysis of the Cosmic Microwave Background (CMB) (from ref. [3]).

At the same time, the matter density extracted from cosmology suggests a large fraction of the matter in the universe to be non-baryonic matter, *i.e.* cold dark matter. Fig. 2 summarizes the findings from supernova explosions of type Ia (SNe), which can be used as "standard candles" to measure the distance via red shift and luminosity in two independent ways, the density fluctuations of galaxy distributions as measure of baryonic acoustic oscillations (BAO) at the time of baryon freeze-out after the big bang, and the analysis of multipole moments in the cosmic microwave background (CMB, see fig. 3 for the results of the PLANCK satellite) [3]. All these findings give a consistent picture with a contribution of 25.9% cold dark matter to the matter density in the universe, and only a contribution of 4.9% of ordinary baryonic matter in the standard ΛCDM model of cosmology (Λ for the cosmological constant and CDM for cold dark matter).

This dark matter puzzle is certainly one of the most pressing problems of today's physics. The nature of dark matter is nevertheless up to now completely unclear. The huge success of quantum field theories for the Standard Model (SM) of particle physics suggests however, that dark matter may be described by similar elementary particle fields. Since dark matter has to be produced during the *same* big bang as the baryonic matter, a residual interaction between dark matter and Standard Model matter seems to be very likely. This approach is currently supported by several popular models for the extension of the Standard Model, *e.g.* Super-Symmetry, which provide naturally candidates for dark matter particles with very weak interaction with ordinary matter.

Several experimental attempts are in progress for the direct detection of such dark matter particles. At high energies, *e.g.* at the LHC, the search for direct production of unknown mas-

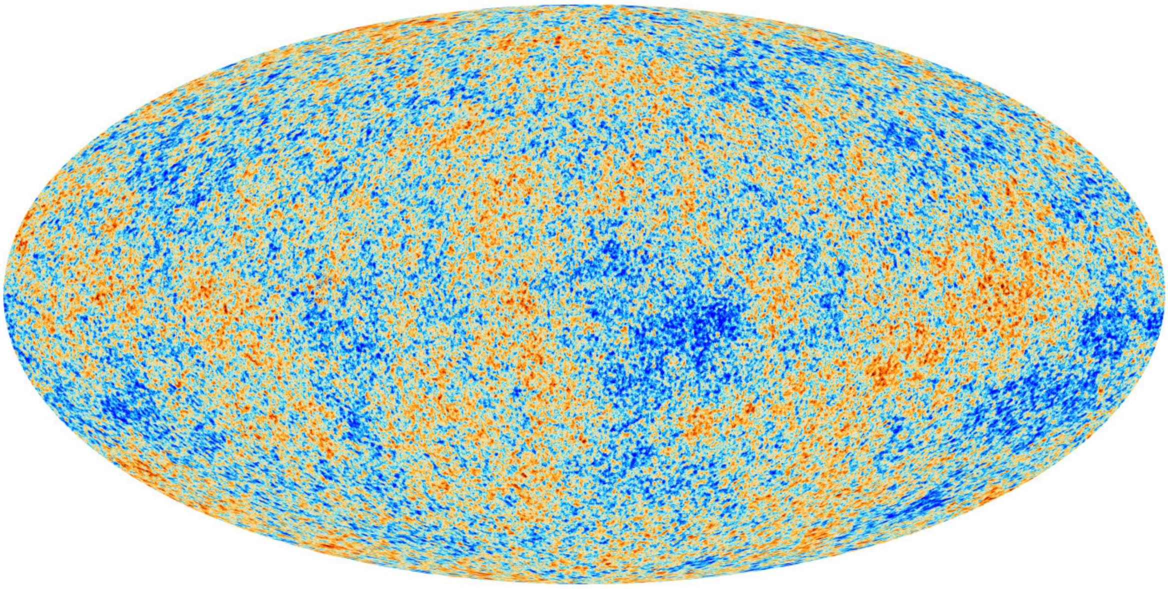

Figure 3: Map of the fluctuations in the Cosmic Microwave Background as seen by the PLANCK satellite. The over-all dipole moment is subtracted.

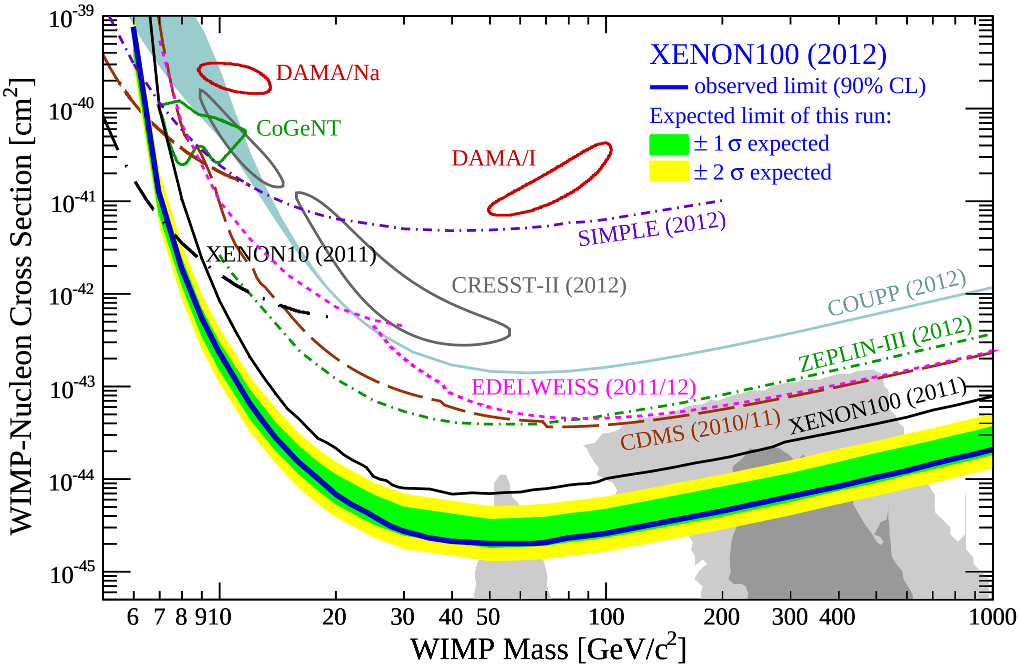

Figure 4: Exclusion limits with direct detection experiments (from ref. [4]).

sive particles is part of the experimental program. At very low energies, the direct detection of scattering processes of dark matter particles with extremely sensitive detectors in well shielded underground laboratories reaches already very sensitive limits in mass range and cross section for the interaction between Standard Model matter and heavy dark matter particles. Fig. 4 shows recent exclusion limits from these direct scattering experiments [4]. This kind of experiment will reach in the next years the limit of the unavoidable background of neutrino-nucleus scattering, up to now without a clear signal of dark matter[1].

The search for dark photons described in this work is complementary to these direct detection experiments. Nearly all extensions of the Standard Model on the basis of field theories suggest larger symmetry groups, leading automatically not to a single “Dark Matter particle” but to a more general “Dark Sector” of hidden particles with a similar rich structure as the Standard Model. A more general approach for the search for dark matter is therefore not to search exclusively for a heavy particle which makes up the mass of the observed dark matter halo, but to test the idea of a “Dark Sector” as a whole.

Assuming the existence of an interaction of the dark sector, it is natural to start the search with the simplest possible (lowest rank) symmetry group. An interaction within the dark sector is carried in these models by a $U(1)$ gauge boson, which is called sometimes “Dark Photon” since it carries the quantum numbers of a photon. Such $U(1)$ symmetries occur naturally in several extensions of the Standard Model, like *e.g.* String Theory. Neglecting all other structure besides the dark photon, it is sufficient to restrict the model structure to

$$U(1)_{\text{dark}} \times \underbrace{U(1)_Y \times SU(2)_{\text{W}} \times SU(3)_{\text{S}}}_{\text{Standard Model}}$$

This is sometimes called the “Vector Portal” to dark matter. Other interactions allowed by Standard Model symmetries with dimensionless couplings are the “Higgs Portal” ($\mathcal{L} = \cdots + \epsilon\,|h|^2|\phi|^2$) and the “Neutrino Portal” ($\mathcal{L} = \cdots + \epsilon\,\epsilon(hL)\psi$, see [5] for an overview.).

---

[1] There are, of course, heavily disputed results of the DAMA and COGENT collaboration which will not be discussed in this work.

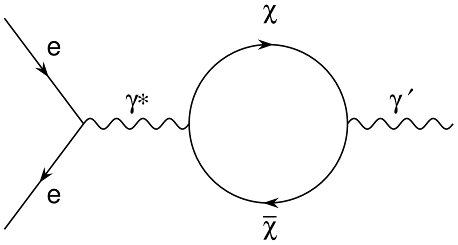

Figure 5: Mixing of the dark photon with the standard model photon.

1.2 Properties of the Dark Photon

A sketch of a possible dark photon interaction with Standard Model matter is given in fig. 5. A virtual photon with the mass of a dark photon interacts with a dark sector particle χ which couples to both kinds of photons. The mechanism of such a mixing was investigated already in 1986 by B. Holdom [6] and is known as kinetic mixing. With weak coupling and at high mass of the dark sector particle χ the process is dominated by the kinetic term of the Lagrangian

$$\mathcal{L} = \cdots - \frac{1}{4} F^{\text{SM}}_{\mu\nu} F^{\mu\nu}_{\text{SM}} - \frac{1}{4} F^{\text{hidden}}_{\mu\nu} F^{\mu\nu}_{\text{hidden}} + \frac{\epsilon}{2} F^{\text{SM}}_{\mu\nu} F^{\mu\nu}_{\text{hidden}} + m^2_{\gamma'} A^{\text{hidden}}_{\mu} A^{\mu}_{\text{hidden}}$$

with a mixing parameter ϵ. Even if the dark sector particle χ is so heavy that it is impossible to be produced, the loop effect might be nevertheless of measurable size.

The mixing term describes the coupling between the electromagnetic field of the Standard Model A^{SM} and the hidden field A^{hidden} and can be interpreted as an effective coupling via

$$\epsilon^2 = \frac{\alpha'}{\alpha}.$$

The mass of the dark photon and the magnitude of the mixing is not given a priory and has to be estimated by models in accordance with observations. Assuming that ϵ vanishes at high energies, ϵ can be generated by perturbative corrections. In Grand Unified Theory, symmetry breaking requires at least two loops, leading to a natural scale of $\epsilon \sim 10^{-8} - 10^{-2}$. Including non-perturbative models, values of $\epsilon \sim 10^{-12} - 10^{-3}$ have been discussed (see *e.g.* [7, 8]).

Several experimental hints support the dark photon hypothesis and give estimates for the parameter range in mass and mixing of the dark photon. One of the most prominent examples is the anomalous magnetic moment of the muon $a_\mu = (g-2)_\mu$. Figure 6 compares the experimental measurement of a_μ by the BNL-E821 experiment [9] with precision QED calculations [10], showing a clear several sigma discrepancy between experiment and theory. Such a discrepancy could be explained by corrections with additional dark photon loops in the coupling of the photon to the muon [11, 12]. Figure 7 shows the range in mixing parameter ϵ and mass $m_{\gamma'}$ of a dark photon which could explain this discrepancy (red line and 2 σ error band), and the interpretation of the $(g-2)$ measurements on electron and muon as exclusion limits.

A further prominent hint comes from the positron excess in the galaxy, first observed by PAMELA [13] and FERMI-LAT [14], and later confirmed with a large statistical sample by AMS-02 [15]. These observations show a clear excess of high-energetic cosmic positrons above the model expectations (Fig. 8). While these model assumptions can be questioned and other models for a positron excess, for example Quasars, are also discussed in the literature, the dark photon annihilation process provides a good fit to the observed positron spectrum. Since no anti-proton excess is observed up to now, this observation favors the mass range $m_{\gamma'} < 2\,m_{\text{proton}}$ of the dark photon.

Several other phenomena are discussed in the literature, including loop effects in the coupling of the photon to the muon explaining the proton radius puzzle. From all models and observations, a parameter range $10^{-3} < \epsilon < 10^{-7}$ and $1\,\text{MeV}/c^2 < m_{\gamma'} < 2\,\text{GeV}/c^2$ is favored.

1.3 Search for Dark Photons with Fixed Target Experiments

Since a dark photon is expected to mix with the Standard Model photon, all processes producing a final state via a virtual photon with a mass in the range of the dark photon mass are well suited for an experimental search. Fig. 9 shows one of the simplest graphs for such a dark photon production. A dark photon is emitted by a high energetic electron in the field of a heavy target nucleus.

The cross section and background of this reaction was first estimated in the Weizsäcker-Williams-Approximation by Bjorken and co-workers [16]. Assuming a decay back to Standard Model matter, the dark photon has a live time of

$$\gamma c\tau \sim 1\ \text{mm}\left(\frac{\gamma}{10}\right)\left(\frac{10^{-4}}{\epsilon}\right)^2\left(\frac{100\,\text{MeV}}{m_{\gamma'}}\right),$$

i.e. a decay length in the range of a few micrometers until several meters for a low mixing parameter. After this flight path it will decay with branching ratios shown in fig. 10 back to standard model

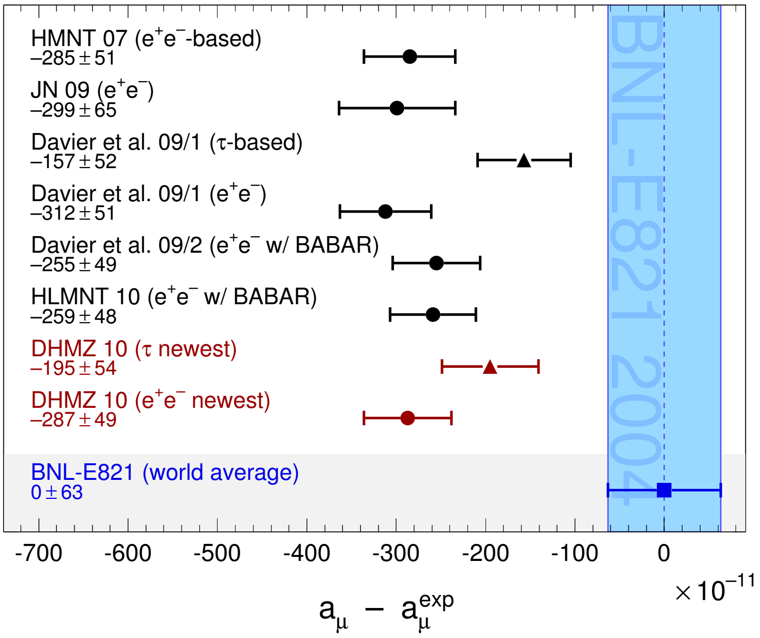

Figure 6: Comparison of the $a_\mu = (g-2)_\mu$ measurement of the BNL-821 experiment with calculations in QED.

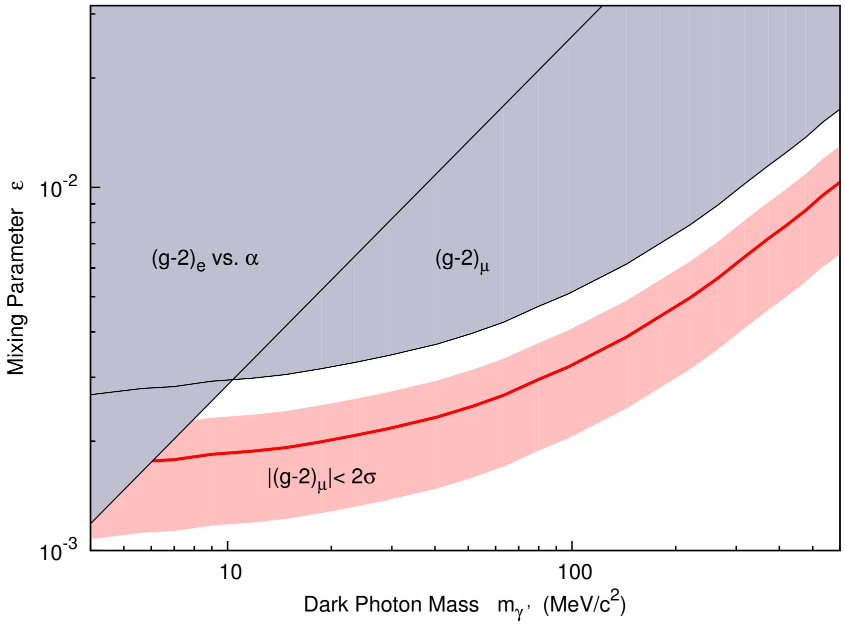

Figure 7: The parameter space in mass and mixing parameter excluded by $(g-2)$ of the electron and the muon (blue shaded area). The red line shows the region of the parameter space, where the discrepancy could be explained by loop effects of dark photons.

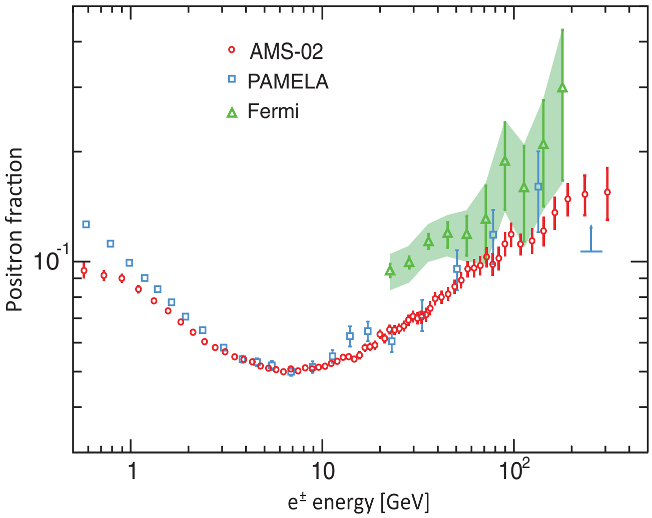

Figure 8: Fraction of positrons to electrons from cosmic rays as measured by Fermi, PAMELA and AMS-02 (from ref. 8). A clear excess can be seen at higher energies.

matter. For the mass range considered in this work, only the decay into an electron or muon pair is relevant.

The experimental signature of a dark photon decay is now a peak in the mass spectrum of the e^+e^- or $\mu^+\mu^-$ pair at the mass of the dark photon.

While the important work of Bjorken and co-workers showed the feasibility of direct search experiments at accelerators, the used Weizsäcker-Williams-Approximation turned out to be not accurate enough to describe the experiments especially in the energy range covered in the later discussed experiments. Therefore signal and background amplitude was calulated in tree level.

Fig. 11 shows the relevant background graphs. Graph (a) and (b), called time-like graphs, since the photon coupling to the incoming electron is time-like, have the same structure for signal and background, the lower (space-like) graphs only apply for the background, since the photon is space-like.

The invariant amplitude for the signal $\mathcal{M}_{\gamma'}^{\mathrm{TL}}$ and time-like ($\mathcal{M}_{\gamma^*}^{\mathrm{TL}}$) and space-like ($\mathcal{M}_{\gamma^*}^{\mathrm{SL}}$) background graphs is given by

$$
\begin{aligned}
\mathcal{M}_{\gamma'}^{\mathrm{TL}} &= \frac{i\, e^4\, \varepsilon^2}{(p'-p)^2} \, \frac{-g^{\alpha\beta} + q'^{\alpha} q'^{\beta}/m_{\gamma'}^2}{q'^2 - m_{\gamma'}^2 + i\, m_{\gamma'}\, \Gamma_{\gamma'}} \, J_N^{\mu}\, \mathcal{I}_{\mu\alpha}\, \overline{u}_l(l_-, s_-)\, \gamma_\beta\, v_l(l_+, s_+), \\
\mathcal{M}_{\gamma^*}^{\mathrm{TL}} &= \frac{i\, e^4}{(p'-p)^2} \, \frac{-g^{\alpha\beta}}{q'^2} \, J_N^{\mu}\, \mathcal{I}_{\mu\alpha}\, \overline{u}_l(l_-, s_-)\, \gamma_\beta\, v_l(l_+, s_+), \\
\mathcal{M}_{\gamma^*}^{\mathrm{SL}} &= \frac{i\, e^4}{(p'-p)^2} \, \frac{-g^{\alpha\beta}}{q^2} \, J_N^{\mu}\, \tilde{\mathcal{I}}_{\mu\alpha}\, \overline{u}_e(k', s_k')\, \gamma_\beta\, u_e(k, s_k).
\end{aligned}
$$

With k and k' momentum of incoming and outgoing scattered electron, p and p' momentum of incoming and outgoing nucleus, l and l' momenta of outgoing lepton pair and $q = k - k'$, $q' = l_+ + l_-$.

The leptonic tensors are given by

$$
\begin{aligned}
\mathcal{I}_{\mu\alpha} &= \overline{u}_e(k', s_k') \left(\gamma_\mu \frac{(\not{k} - \not{q}') + m_l}{(k-q')^2 - m_l^2} \gamma_\alpha + \gamma_\alpha \frac{(\not{k}' + \not{q}') + m_l}{(k'+q')^2 - m_l^2} \gamma_\mu \right) u_e(k, s_k), \\
\tilde{\mathcal{I}}_{\mu\alpha} &= \overline{u}_l(l_-, s_-) \left(\gamma_\mu \frac{(\not{q} - \not{l}_+) + m_l}{(q-l_+)^2 - m_l^2} \gamma_\alpha + \gamma_\alpha \frac{(\not{l}_- - \not{q}) + m_l}{(l_- - q)^2 - m_l^2} \gamma_\mu \right) v_l(l_+, s_+).
\end{aligned}
$$

The hadronic current is given by $J_N^{\mu} = Z \cdot F(Q_t) \cdot (p + p')^{\mu}$ where we used the form factor of a solid sphere as nuclear form factor $F(Q_t)$. The background graphs for producing an electron positron

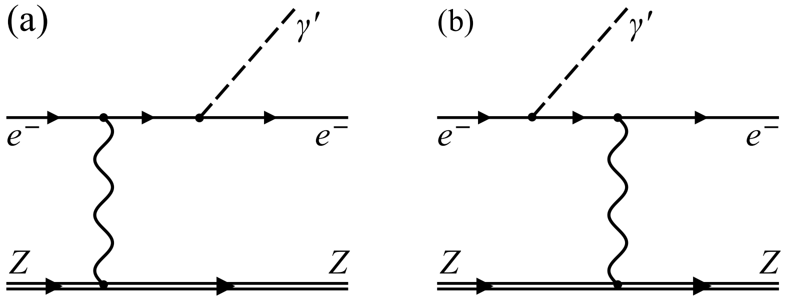

Figure 9: Radiative production of a dark photon from final (a) and initial (b) electron line.

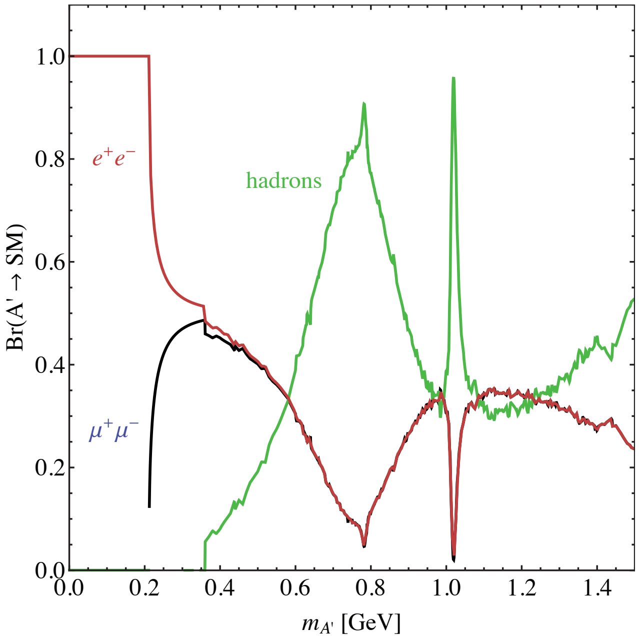

Figure 10: Branching ratios of the decay of a dark photon to Standard Model matter. The $\rho(770)$ and $\phi(1020)$ peaks dominate the hadron spectrum.

pair have to be antisymmetrized in respect to the exchange of scattered electron and electron of the pair.

$$\mathcal{M}_{\gamma^*} = \mathcal{M}_{\gamma^*}^{\mathsf{TL}} + \mathcal{M}_{\gamma^*}^{\mathsf{SL}} - (\mathcal{M}_{\gamma^*}^{\mathsf{TL}} + \mathcal{M}_{\gamma^*}^{\mathsf{SL}})(k' \leftrightarrow l_-)$$

The differential cross section is now given in the laboratory frame by

$$\frac{d^9\sigma}{dm_{ll}\, dE'\, d\Omega'\, dq'\, d\Omega_{q'}\, d\Omega_+} = \frac{E'}{E_0} \frac{\sqrt{(s-(M-m_{ll})^2)\,(s-(M+m_{ll})^2)}\sqrt{m_{ll}^2 - 4m_l^2}}{128M\,(2\pi)^8\, 2\, s}\, \overline{|\mathcal{M}|^2},$$

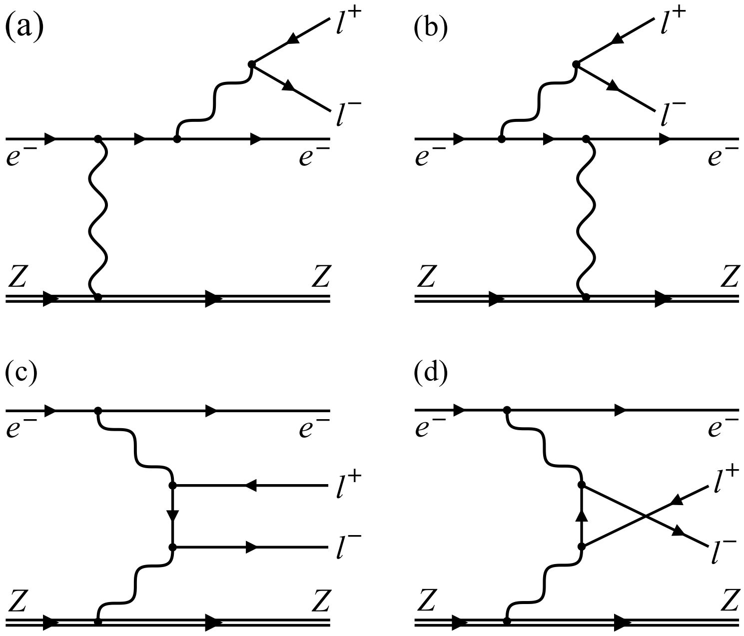

Figure 11: Dominant background graphs.

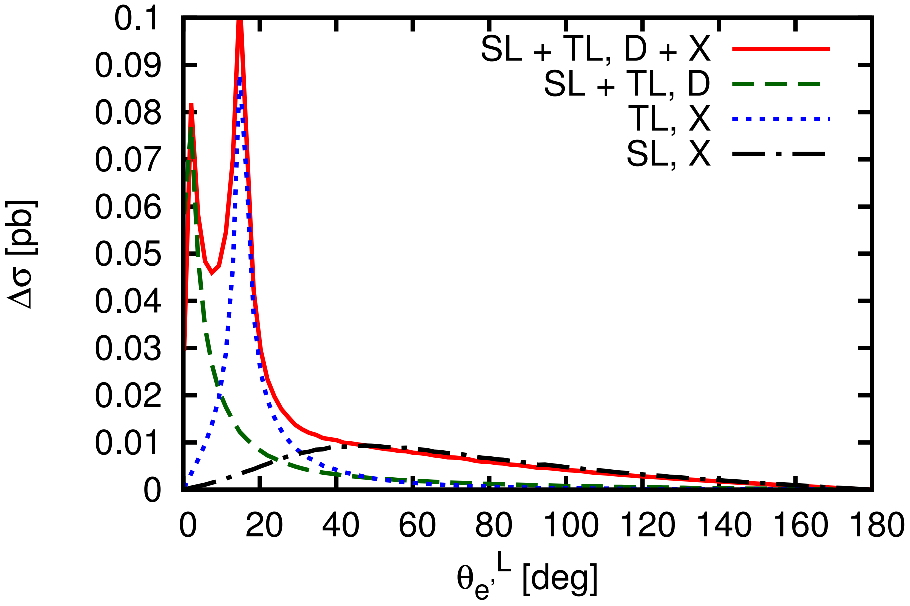

Figure 12: Example of the angular distribution of the polar angle of the scattered electron. “D” denotes the contribution of the direct graphs, while “X” denotes the anti-symmetrized (exchange) graphs. The clear peak added by the anti-symmetrization can be seen.

with the pair momentum q' and solid angle $d\Omega_{q'}$ in the photon-target rest frame, and the decay solid angle $d\Omega_{+}$ in the pair rest frame.

It is straight forward to calculate the 9-fold cross section. The experiment however integrates over the undetected outgoing electron and recoil nucleus. This integration is prone to numerical instabilities and introduces a huge statistical variance of the result due to the pole structure of the cross section. Especially in the space-like background graphs the intermediate electron can be close to mass shell and for the anti-symmetrized time-like graphs the virtual photon can be close to mass shell. Fig. 12 shows as an example the cross section in dependence of the polar angle of the scattered electron in respect to the beam direction for one of our used kinematic settings. The peak of the anti-symmetrization graphs can be clearly seen. There is, fortunately, no true divergence in the cross section, since the electron mass serves as regulator for the peaks.

The numerical integration was performed in parallel with two strategies. A “hand optimized” generator was developed running on a conventional CPU. In parallel, a program using an automatic Monte Carlo algorithm (VEGAS) was developed using the parallelization of graphics processing units (NVIDIA CUDA framework). Both calculations agree within their standard deviation which is below 10^{-4} of the calculated value[17].

1.4 Experiments at MAMI

The experimental challenge of a fixed target search for dark photons is to be sensitive for a tiny peak in the invariant mass of a lepton pair on top of overwhelming background of QED pair-production. It is obvious, that besides the capability to run at a huge luminosity the resolution in

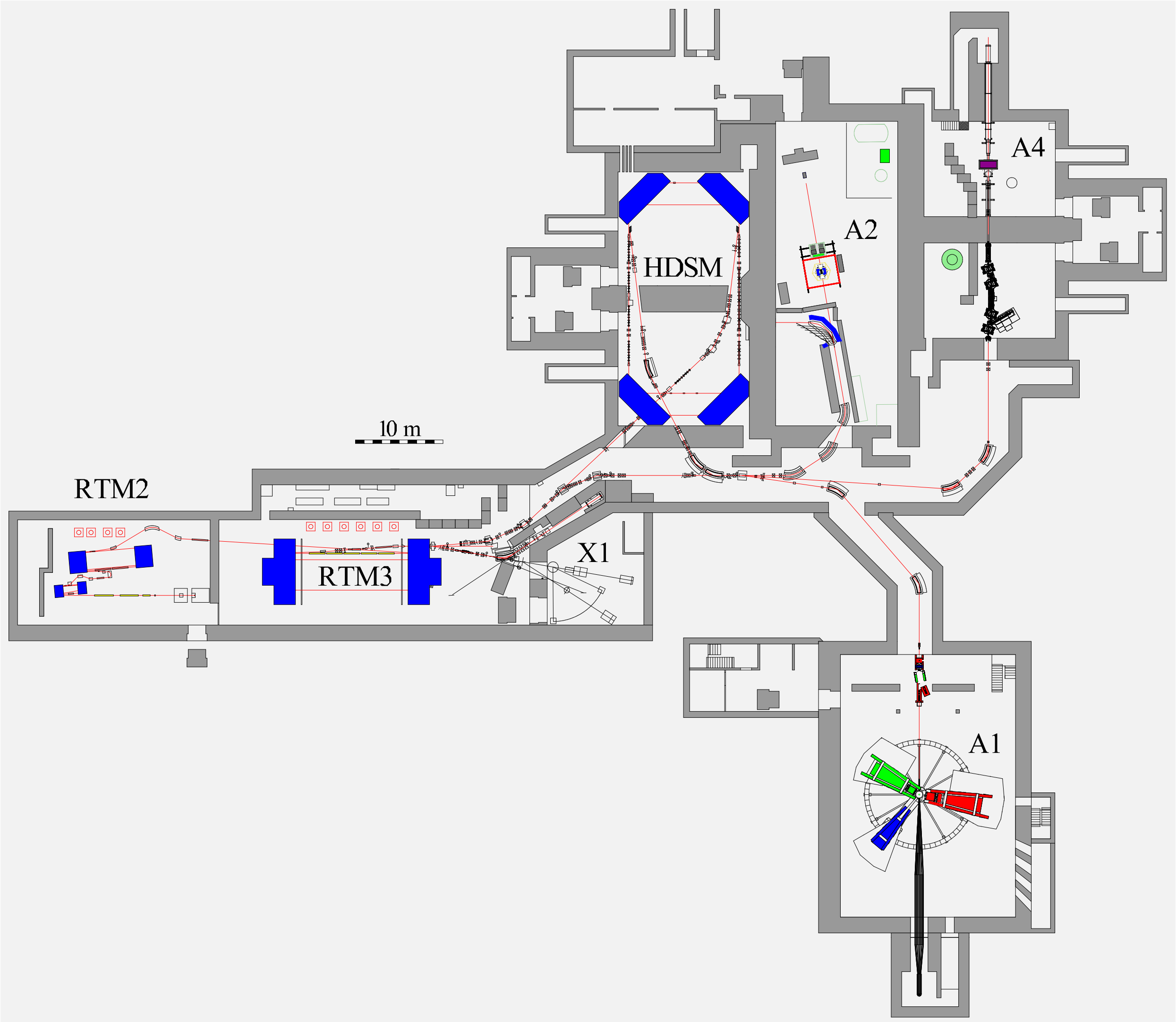

Figure 13: Floor plan of the Mainz Microtron (MAMI).

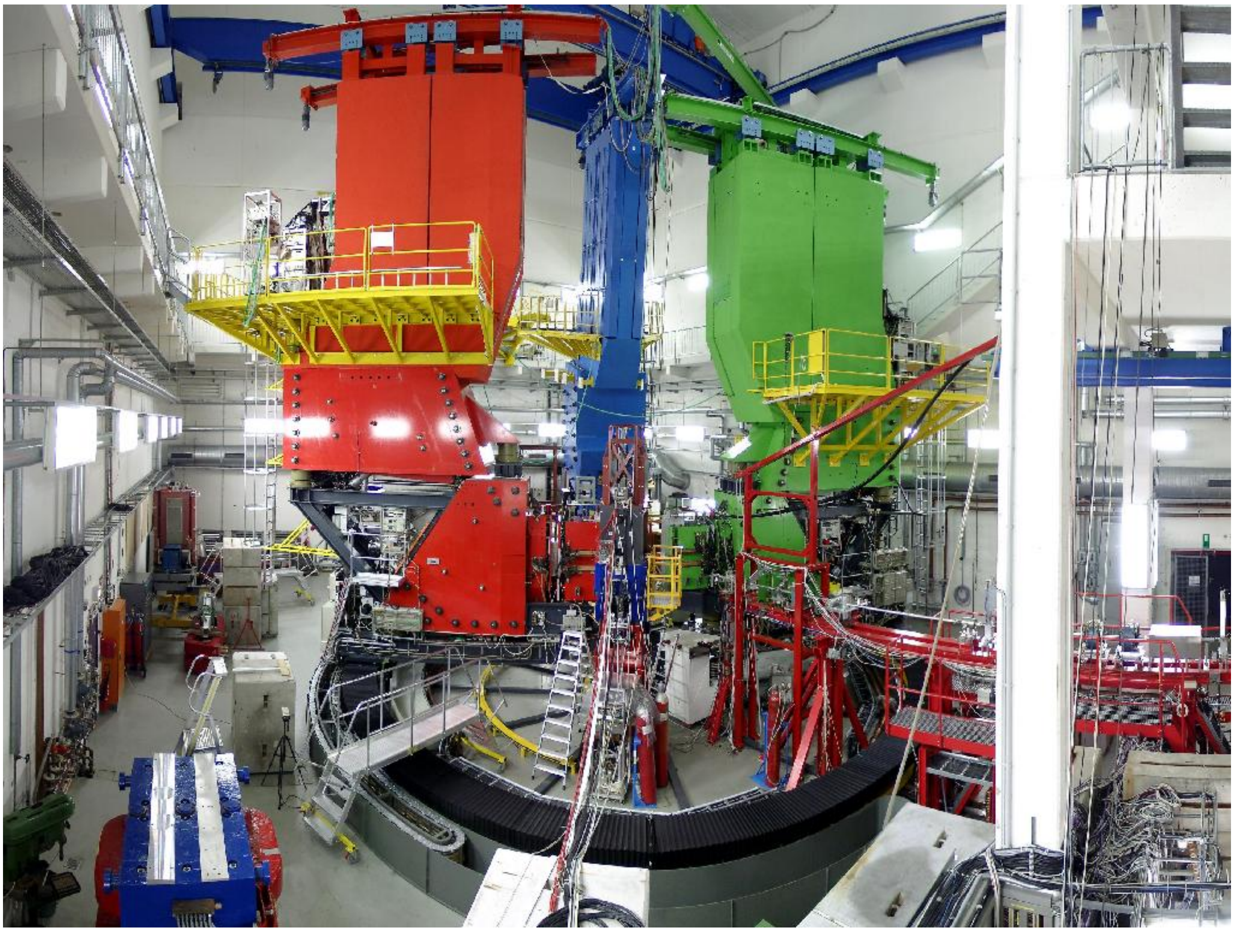

Figure 14: The spectrometer setup of the A1 Collaboration.

the determination of the peak is the most important constraint of the experiment. While the signal-to-background ratio goes with the square root of the luminosity, the resolution enters linearly.

The Mainz Microtron (MAMI) is ideally suited for this kind of experiment due to the excellent beam quality of the Microtron principle. Fig. 13 shows the floor plan of MAMI, which consists of a cascade of several microtrons. After a 4 MeV linear accelerator, the first stage reaches within 18 recirculations a beam energy of 15 MeV, the second stage reaches with 51 recirculations a beam energy of 180 MeV. This is the lowest energy for extracted beam. With the third stage up to 855 MeV can be reached in energy steps of 15 MeV with up to 90 recirculations.

The excellent beam quality can be seen by the horizontal emittance of $13\pi \cdot \mu\mathrm{m} \cdot \mathrm{rad}\ (1\sigma)$ and a vertical emittance of only $0.84\pi \cdot \mu\mathrm{m} \cdot \mathrm{rad}\ (1\sigma)$.

A beam current of up to $100\,\mu\mathrm{A}$ can be reached, and the luminosity for these experiments can be tuned by the choice of the target thickness and is limited by resolution effects, the rate capability of the detectors, and the over all radiation in the hall.

1.4.1 The Spectrometer Setup of the A1 Collaboration

The A1 Collaboration operates the spectrometer setup at MAMI and uses the beam of MAMI for electron scattering experiments [18]. The setup consists of three standard spectrometers (de-

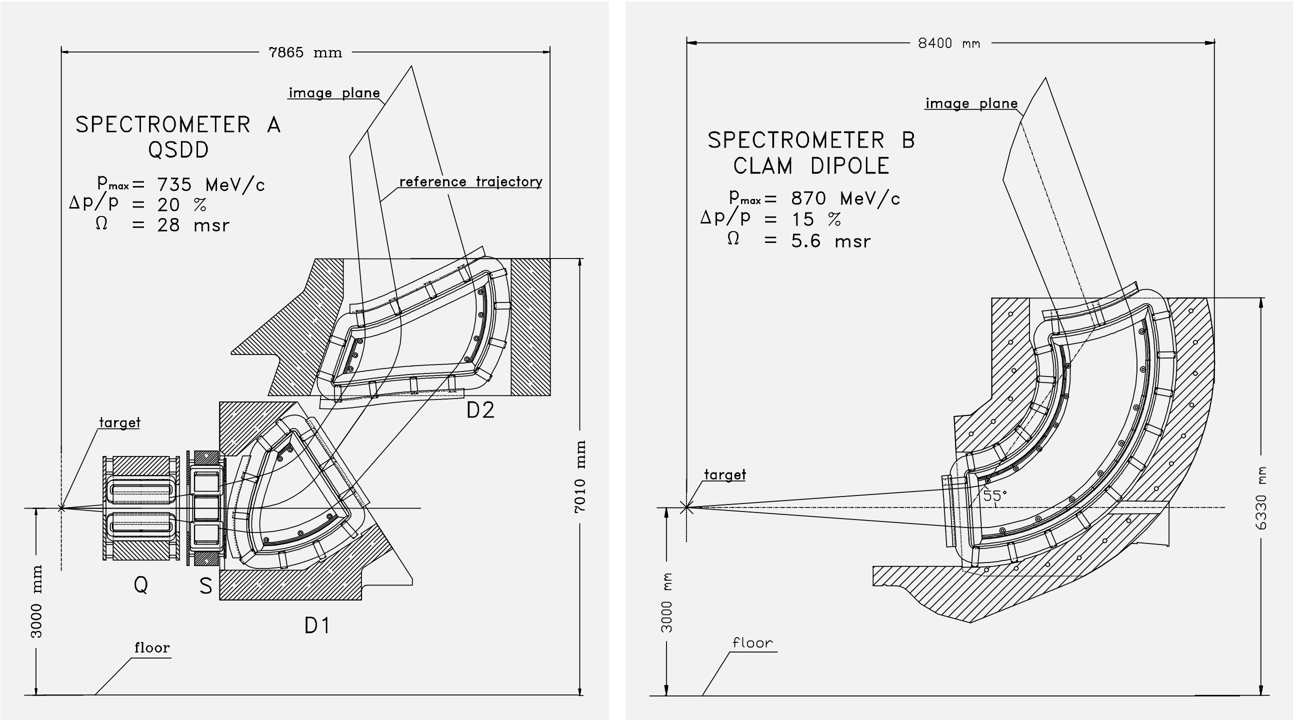

Figure 15: Magnet optics of spectrometer A and B.

noted A, B, and C) and can be extended with a Kaon spectrometer (KAOS) and a short-orbit spectrometer (SOS) for low-energetic pions.

For the dark photon search, spectrometer A and B were used for the detection of the electron-positron pair (red and blue in fig. 14). Fig. 15 shows the magnet-optical design of these two spectrometers. Spectrometer A consists of a non-dispersive focusing quadrupole magnet and a sextupole magnet for higher order corrections. Two dipole magnets give a dispersion of $5.77\,\mathrm{cm}/\%$ and provide the dispersive focusing by the shape of the entrance and exit edge of the pole pieces. The whole system provides point-to-point transformation in the dispersive plane and a parallel-to-point transformation in the non-dispersive plane. Spectrometer B consists of a single dipole magnet. The pole pieces are tilted around the axis through target point and focal plane for non-dispersive point-to-point focusing ("Clamshell-Dipole"), the dispersive focusing is again provided by the shape of the pole pieces. The dispersion of spectrometer B is $8.22\,\mathrm{cm}/\%$.

Both spectrometers are equipped with a package of focal plane detectors consisting of four layers of vertical drift chambers for position and angular resolution and two layers of scintillators for trigger and timing purposes. Additional threshold Čerenkov detectors discriminated between electrons and pions.

Over all, the spectrometers reach a momentum resolution of better than $\Delta p/p = 10^{-4}$ and an angular resolution of better than 3 mrad. The angular acceptance of spectrometer A is 28 msr and of spectrometer B, due to the clamshell design, 5.6 msr. The momentum acceptance of spectrometer A is 20% and of spectrometer B is 15%.

Tabelle 1: Kinematic settings. The incident beam energy was $E_0 = 855\,\mathrm{MeV}$, and the settings are roughly centered around $E_{e^+} + E_{e^-} = E_0$ and $m_{\gamma'} = 250\,\mathrm{MeV}/c^2$.

	Spec. A (e^+)			Spec. B (e^-)			
	p (MeV)	θ	$d\Omega$ (msr)	p (MeV)	θ	$d\Omega$ (msr)	Events
Setup 1	346.3	22.8°	21	507.9	15.2°	5.6	208×10^6
Setup 2	338.0	22.8°	21	469.9	15.2°	5.6	47×10^6

1.4.2 First Pilot Experiment

In 2011, a first test experiment was performed [19]. In this test, the feasibility and sensitivity of the A1 apparatus for dark photon searches was investigated.

The kinematic setup was chosen for maximum sensitivity. The production cross section of dark photons peaks in the direction of the incoming beam. At the same time, the cross section peaks, if the complete beam energy is transferred to the dark photon, *i.e.* the scattered electron remains at rest. Using the maximum energy of the second stage of MAMI of $E_0 = 855\,\mathrm{MeV}$ this defines the kinematics (setup 1 of table 1). During the measurement, which was designed using the approximations of ref. [16], it was realized, that a slight modification to lower energy transfers increases the sensitivity. This was done in setup 2 of table 1. Both settings result in a sensitivity in the mass range of $200\,\mathrm{MeV}/c^2 < m_{\gamma'} < 320\,\mathrm{MeV}/c^2$.

Tantalum was chosen as target nucleus ($Z = 73$). Tantalum is easy to handle and is with a natural fraction of 99.9% of $^{181}\mathrm{Ta}$ nearly mono-isotopic, which can be utilized for resolution calibration by measuring the elastic line spectrum of Tantalum. The mass resolution depends on the angular resolution of the electron and positron detection. Therefore the multiple scattering in the target foil had to be minimized by using a Target consisting of 12 strips of Tantalum with a total area density of $81.3\,\mathrm{mg/cm}^2$. The strips were 1 mm wide with 1 cm spacing, ensuring that the outgoing electrons and positrons hit no further strip. All in all, a pair mass resolution of better than $0.5\,\mathrm{MeV}/c^2$ was achieved.

The electrons and positrons were identified by the threshold Čerenkov detectors of the spectrometers. In a second step, the coincidence time was corrected for the flight path in the spectrometers. A coincidence time peak with a width of $1\,\mathrm{ns}$ (FWHM) could be achieved. By using the side bands of the coincidence time spectrum, the amount of accidental coincidences could be estimated to be around 5%.

No peak was detected in the mass spectrum of the electron-positron pair. Using a sliding average of the neighboring bins as background estimation, a Feldman-Cousins algorithm was used to determine exclusion limits for the dark photon production cross section. Since the absolute luminosity calculation was questionable due to the strip structure of the target, we used Eq. (19) of Ref. [16]

$$\frac{d\sigma(X \to \gamma' Y \to e^+e^- Y)}{d\sigma(X \to \gamma^* Y \to e^+e^- Y)} = \frac{3\pi}{2N_\mathrm{f}} \frac{\epsilon^2}{\alpha} \frac{m_{\gamma'}}{\delta_m},$$

i.e. the ratio of dark photon cross section to QED pair production to extract the mixing parameter ϵ. In this equation, N_f is the ratio of phase space for the decay to an electron-positron pair (1

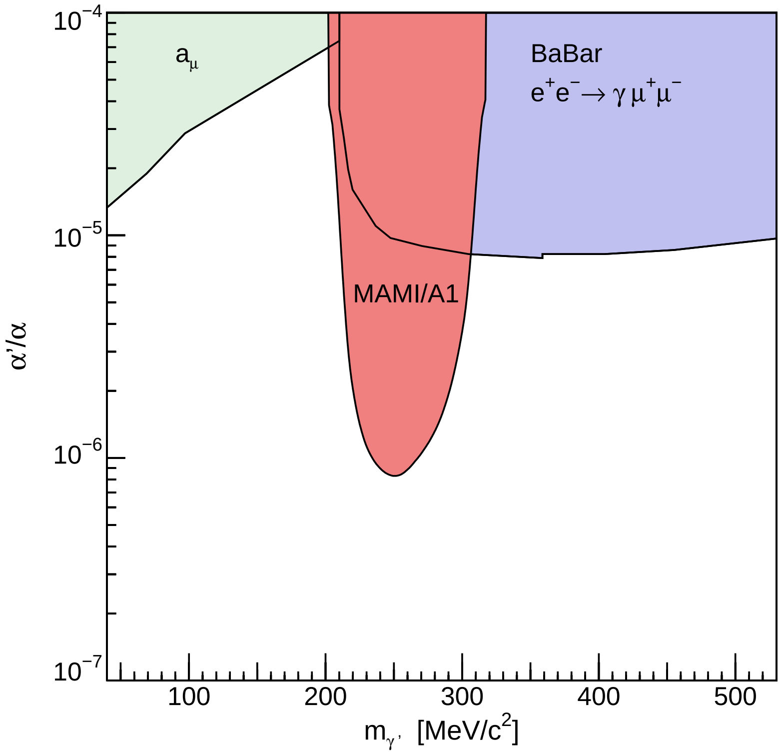

Figure 16: The exclusion plot of the first test experiment.

below two muon threshold), α is the fine structure constant, and δ_m is the mass resolution of the detection.

Fig. 16 summarizes the exclusion limit derived from the first test experiment. Also drawn are the standard model prediction of the anomalous magnetic moment of the muon [12] and a reanalysis [20] of data of the BaBar collaboration [21].

Already in this test measurement, the exclusion limit could be extended by nearly one order of magnitude. Shortly after the MAMI experiment, a similar pilot experiment was performed by the APEX collaboration at Jefferson Laboratory [22] with similar results.

1.4.3 Extended Mass Range

To cover an extended mass range with the A1 spectrometer setup, the incoming beam energy has to be varied in several steps. The lowest possible beam energy is given by the end-point energy of the second microtron stage with $E_0^{\text{min}} = 180\,\text{MeV}$. This minimal energy in combination with the minimum angles of the spectrometers restrict possible experiments at A1 to a dark photon mass $m_{\gamma'} > 50\,\text{MeV}/c^2$. The maximum mass is in principle given by the end-point energy of the third stage of MAMI (MAMI C) of $E_0^{\text{max}} = 1508\,\text{MeV}$. The count rate is however very small at this energy due to the large minimal angles of the spectrometers. In addition, the absolute energy calibration of the third stage is not known to sufficient accuracy to combine data of the second stage with data from the third stage. Therefore, an experiment was designed using only the second stage with an end-point energy of $855\,\text{MeV}$ to cover the mass range of $50\,\text{MeV}/c^2 < m_{\gamma'} < 300\,\text{MeV}/c^2$, the range most important to test the region of the $(g-2)$ anomaly of the muon.

Tabelle 2: Kinematic settings. All settings were centered around the production of lepton-pairs in beam direction and with maximum energy transferred to the pair.

	$m_{\gamma'}$ (MeV/c^2)	E_0 (MeV)	θ_{e+}	p_{e+} (MeV/c)	θ_{e-}	p_{e-} (MeV/c)	e^+ in Spec.	e^- in Spec.	$d\Omega_A$ (msr)	$d\Omega_B$ (msr)	Target
1	54	180	20.0°	74.0	15.1°	97.1	A	B	28	5.6	single foil
2	54	180	15.1°	100.3	20.0°	74.0	B	A	21	5.6	single foil
3	57	180	20.0°	78.7	15.6°	98.0	A	B	21	5.6	single foil
4	72	240	20.0°	103.6	15.6°	132.0	A	B	21	5.6	single foil
5	76	255	20.0°	105.0	15.1°	137.3	A	B	28	5.6	single foil
6	77	255	20.0°	110.1	15.6°	140.4	A	B	21	5.6	single foil
7	91	300	20.0°	129.5	15.6°	164.6	A	B	21	5.6	single foil
8	103	345	20.0°	142.0	15.1°	186.5	A	B	28	5.6	foil stack
9	109	360	20.0°	155.4	15.6°	197.6	A	B	21	5.6	single foil
10	135	450	20.0°	185.0	15.1°	243.3	A	B	28	5.6	foil stack
11	138	435	15.6°	244.0	20.0°	190.7	B	A	21	5.6	single foil
12	138	435	15.6°	233.9	20.0°	190.0	B	A	21	5.6	single foil
13	138	435	20.0°	190.0	15.6°	244.5	A	B	21	5.6	single foil
14	138	435	20.0°	190.0	15.6°	234.1	A	B	21	5.6	single foil
15	150	495	20.0°	213.7	15.6°	271.1	A	B	21	5.6	foil stack
16	170	570	20.0°	234.0	15.1°	307.3	A	B	28	5.6	foil stack
17	177	585	20.0°	250.0	15.6°	317.3	A	B	21	5.6	foil stack
18	202	675	15.1°	367.0	20.0°	277.2	B	A	21	5.6	single foil
19	218	720	20.0°	309.2	15.6°	392.7	A	B	21	5.6	foil stack
20	256	855	20.0°	351.0	15.1°	460.3	A	B	28	5.6	foil stack
21	270	855	15.2°	509.4	22.8°	346.3	B	A	21	5.6	single foil
22	270	855	15.1°	511.7	20.0°	346.3	B	A	21	5.6	single foil

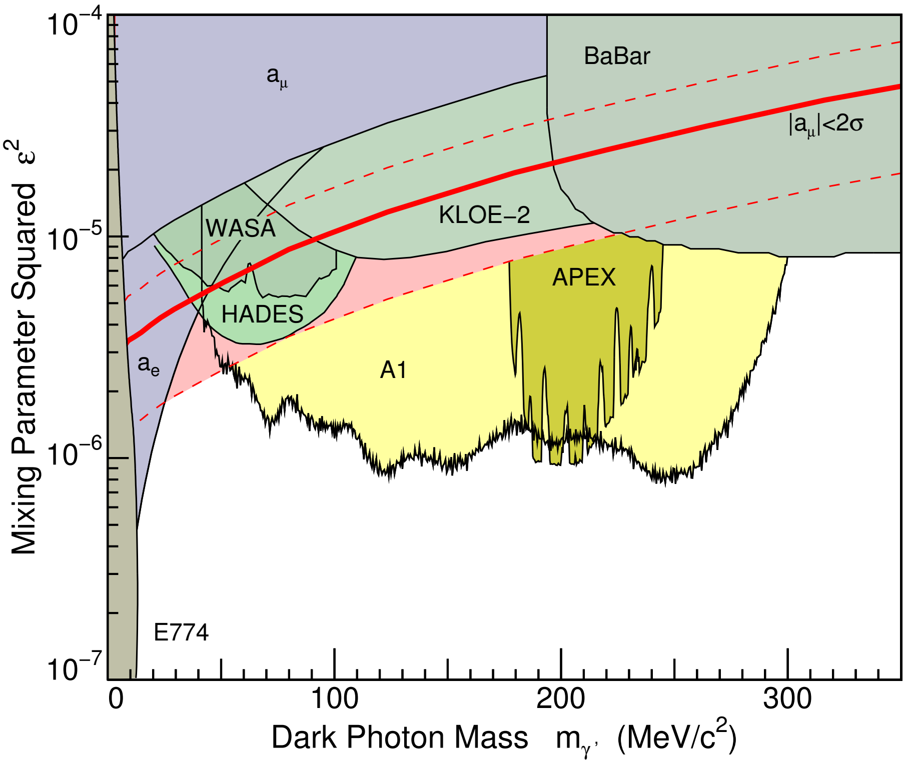

Figure 17

Table 2 summarizes the settings of this experiment. The settings were chosen to optimize the coverage in mass range. While the dark photon production cross section is symmetric under exchange of electron and positron, the background graphs are not due to different antisymmetrization contributions. Therefore different polarities were chosen. Where possible, a single tantalum foil were used. For the high luminosity settings a foil stack similar to the pilot experiment was used.

The analysis was performed similar to the analysis of the pilot experiment (see section 1.4.2) with a few improvements:

- At low masses the shape of the QED background is not well described by a sliding average method. Therefore a local fit of a cubic polynomial was used as background model.
- The new improved background calculations [17] were used for the extraction of the exclusion limits in terms of the mixing parameter ϵ.
- Special care has to be taken to add up several settings to determine a combined exclusion limit. To make sure, that the mass calibration of each setting is better than the resolution, extended calibration measurements of the elastic lines of Tantalum were included.
- The data of the first pilot experiment are included in the whole data sample.

Fig. 17 shows the result of the experiment [23]. An exclusion limit in the mass range $50\,\mathrm{MeV}/c^2 < m_{\gamma'} < 300\,\mathrm{MeV}/c^2$ and down to an mixing parameter squared of $\epsilon^2 = 10^{-6}$ could be derived (yellow shaded region). In addition to the $(g-2)$ bands of fig. 7 and the BaBar results of fig. 16 the results of the APEX collaboration ([22] are included (dark yellow shaded region). Also included are recent results of the WASA-at-COSY [24], KLOE-2 [25], and HADES collaboration [26].

As can be seen, nearly the complete band of the parameter space where the discrepancy between the measurement of the anomalous magnetic moment of the muon $(g-2)$ with standard model expectations could be explained by a dark photon could be excluded by this measurement. A small region below a dark photon mass of $50\,\mathrm{MeV}/c^2$ still is not excluded, however new results of the NA48/2 Collaboration will probably cover this region in the near future[27].

1.5 Summary and Outlook

In this work, new sensitive limits for the existence of dark photons could be derived in the mass range $50\,\mathrm{MeV}/c^2 < m_{\gamma'} < 300\,\mathrm{MeV}/c^2$. The formalism to calculate the production amplitude and the relevant background amplitudes were developed and used to analyze the experiments with high quality event generators.

These experiments cannot be extended in a simple way *e.g.* by increasing the beam time, even an order of magnitude in time will be barely visible on the logarithmic scale of the presented exclusion limits, only a small extension in mass range would be possible by using the higher end-point energy of the third microtron stage.

In this section, other concepts for the extension of a dark photon program in Mainz are discussed.

1.5.1 Displaced Vertex

The method of searching a mass peak on top of a huge QED background is limited by statistics. One can improve the limits by several orders of magnitude in ϵ if one can suppress the QED background. A very clear distinction between dark photon production and QED background is given by the decay length of the dark photons. If one is able to clearly identify a secondary vertex, the background could be eliminated in principle completely.

Several groups are trying to design experiments for the detection of this secondary vertex. All experiments common is the problem, that one has to trade off the use of detectors very close to the vertex, which improves the vertex resolution, with the use of detectors in some distance of the vertex, which improves the rate capability of the detectors at the required high luminosities. The HPS collaboration at JLab, as an example for the first strategy, has designed an experiment using micro-strip detectors very close to the target.

At A1, first attempts were made to identify a secondary vertex by shielding of the primary vertex. In this experiment, the target is moved upstream out of the vertex acceptance of the spectrometers. The production vertex is shielded by lead or tungsten collimators, and the spectrometers are sensitive to the appearance of a lepton pair in the unshielded region.

First tests were done at A1, showing that the method is working in principle. However a certain level of background remained due to back-scattering of Møller-scattering and elastic events from the shielding, which was as close as 5 mm to the target point. Since the background has to be eliminated completely, further work has to be done, and a full scale simulation seems to be unavoidable. Fig. 18 shows the exclusion limits, which can be reached at A1 if the background can be suppressed completely and a decay length between 1 cm and 6 cm is visible by the spectrometers.

1.5.2 Low Energy Accelerator: MESA

Currently, a new accelerator will be constructed in Mainz. The accelerator will consist of superconducting cavities and will reach an energy of 200 MeV. An experiment is planned to use the high current of this accelerator for parity violating electron scattering with extracted beam and external target.

In addition the MESA accelerator is designed to use energy recovery for high currents on an internal target. For this, the recirculating arcs will be entered in the last turn with a phase shift of 180° of the accelerating frequency. The beam will now enter the cavities in the decelerating phase, returning nearly all energy of the beam back to the HF field. Using this technique, a maximum current in the order of several milliampere on an internal target is possible.

The energy recovery mode opens a window to new precision experiments. The low target density, but nevertheless high luminosity, creates the opportunity for high resolution electron scattering experiments in the low energy regime, which would suffer otherwise from multiple scattering and energy loss in target and target walls.

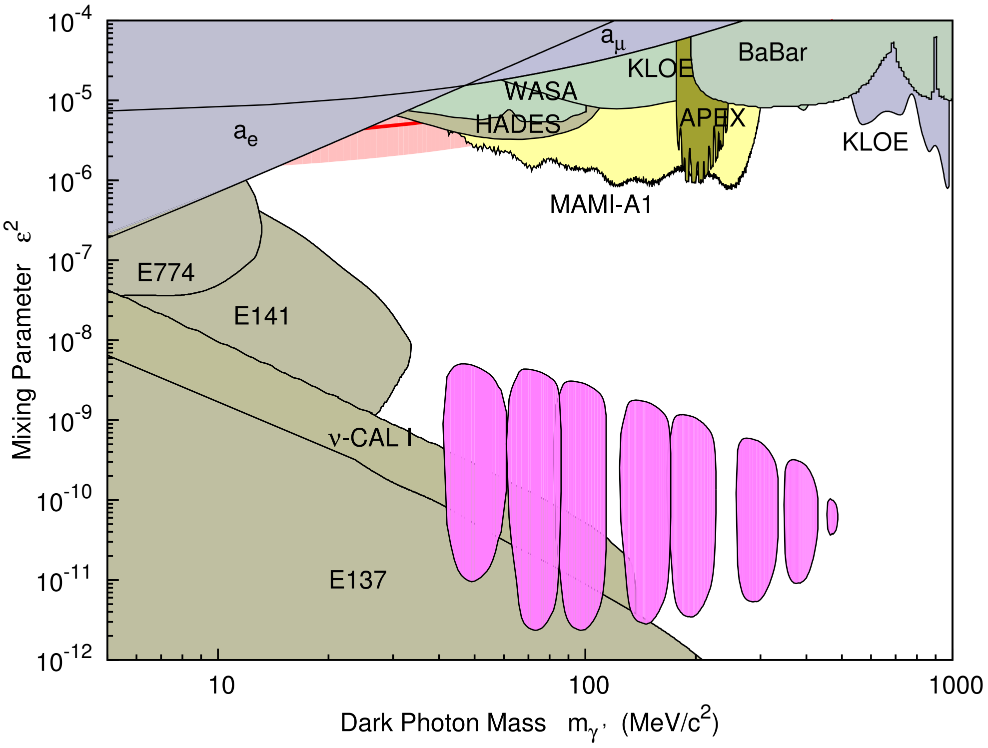

Figure 18: Simulation of exclusion limits for an experiment with shielded primary vertex. Two weeks of beam time were assumed for each area.

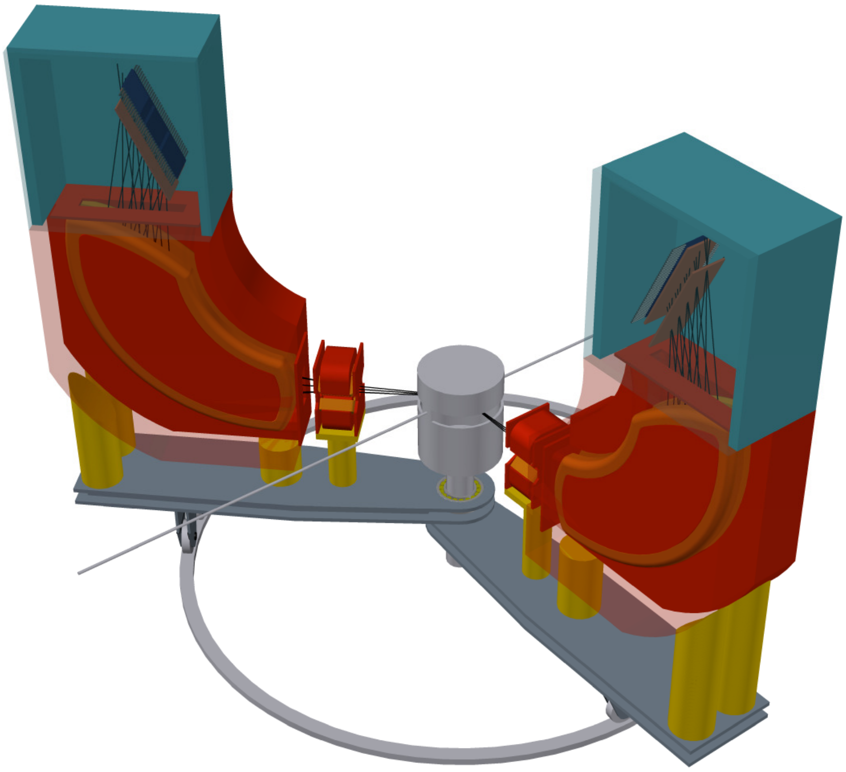

Figure 19: A design study to equip the MESA accelerator with an internal target experiment with two high resolution spectrometers.

Due to the rapid variation of electron scattering cross sections, precision experiments are in general only possible with high resolution spectrometers. A possible design to equip the internal target facility of MESA with two high resolution spectrometers was studied in a Diploma thesis [28], see fig. 19.

In this thesis, the magneto-optical design was calculated with finite-elements methods and resolution and acceptance of the spectrometers were determined with some conservative estimates for resolution and the performance of possible focal plane detectors.

Finally, a possible experiment for the search for dark photons in the low mass region was simulated using the determined acceptances and resolutions with the event generator developed for the MAMI experiments. Fig. 20 shows the resulting sensitivity which could be reached with the MESA accelerator equipped with two high resolution spectrometers within three months of beam-time. A mass range of $8\,\mathrm{MeV}/c^2 < m_{\gamma'} < 60\,\mathrm{MeV}/c^2$ and a mixing parameter squared of down to 10^{-8} can be reached.

1.5.3 Search for Dark Photons with Hidden Decay

All exclusion plots shown so far assume, that the dark photon decays dominantly back to standard model matter. If a particle of the dark sector exists with less than half the mass of the dark photon and with a coupling without kinetic mixing to the dark photon, the corresponding decay would be basically invisible for current experiments.

The negligible target density of the internal target experiment at the MESA accelerator will

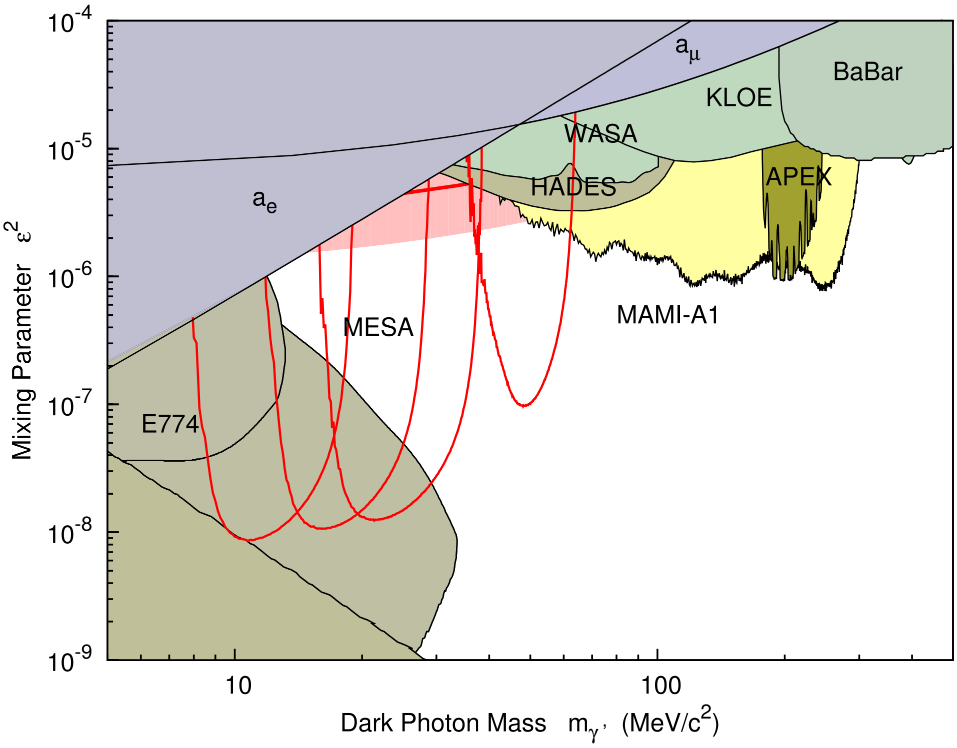

Figure 20: Simulation of exclusion limits calculated with the current design of two spectrometers operated at the MESA accelerator.

enables us to search for dark photons with invisible decay. For this experiment, a light gas target without nuclear excitation will be used, *e.g.* Hydrogen or Helium. The low target density allows to detect the recoil target nucleus in coincidence with the scattered electron with the required high resolution. The dark photon now would show up as peak in the missing mass given by the four momentum balance:

$$m_{\gamma'}^2 = (p_{\text{beam}} - p_{\text{target}} - p_{e'})^2$$

The dominant background of this process will be the radiative tail of virtual Compton scattering.

1.5.4 Beam dump experiments

Assuming an invisible decay of the dark photon, every beam dump of an electron beam basically produces a strong collimated beam of dark matter particles. At the moment, an extension hall for the MESA accelerator is proposed which will be placed behind the beam dump of the parity violating experiment, offering a unique opportunity for a beam dump experiment.

Such an experiment basically has to discriminate between neutrons and light dark matter particles via recoil detection. The standard techniques of the direct dark matter search experiments can be applied, but basically a large volume neutron detector with pulse height analysis as under construction at the A1 collaboration is sufficient for this discrimination and could be installed for operation during the running period of the parity violation experiment.

References

[1] F. Zwicky, On the Masses of Nebulae and of Clusters of Nebulae, Ap. J. 86 (1937) 217. `doi:10.1086/143864`.

[2] E. Corbelli, P. Salucci, The extended rotation curve and the dark matter halo of M33, Monthly Notices of the Royal Astronomical Society 311 (2) (2000) 441–447. `doi:10.1046/j.1365-8711.2000.03075.x`.

[3] N. Suzuki, *et al.*, The Hubble Space Telescope Cluster Supernova Survey, ApJ 746 (2014) 85.

[4] E. Aprile, *et al.*, Dark Matter Results from 225 Live Days of XENON100 Data, Physical Review Letters 109 (18) (2012) 181301. `arXiv:1207.5988`, `doi:10.1103/PhysRevLett.109.181301`.

[5] R. Essig, J. A. Jaros, W. Wester, P. H. Adrian, S. Andreas, *et al.*, Working Group Report: New Light Weakly Coupled Particles (2013). `arXiv:1311.0029`.

[6] B. Holdom, Two U(1)'s and Epsilon Charge Shifts, Phys. Lett. B166 (1986) 196. `doi:10.1016/0370-2693(86)91377-8`.

[7] N. Arkani-Hamed, N. Weiner, LHC Signals for a SuperUnified Theory of Dark Matter, J. High Energy Phys. 12 (2008) 104. `doi:10.1088/1126-6708/2008/12/104`.

[8] R. Essig, P. Schuster, N. Toro, Probing Dark Forces and Light Hidden Sectors at Low-Energy e+e- Colliders, Phys. Rev. D80 (2009) 015003. `doi:10.1103/PhysRevD.80.015003`.

[9] G. W. Bennett, *et al.*, Final report of the E821 muon anomalous magnetic moment measurement at BNL, Phys. Rev. D73 (7) (2006) 072003. `doi:10.1103/PhysRevD.73.072003`.

[10] M. Davier, *et al.*, Reevaluation of the Hadronic Contributions to the Muon $g-2$ and to $\alpha(m_Z)$, Eur. Phys. J. C71 (2011) 1515. `doi:10.1140/epjc/s10052-012-1874-8,10.1140/epjc/s10052-010-1515-z`.

[11] P. Fayet, U-boson production in e^+e^- annihilations, ϕ and υ decays, and light dark matter, Phys. Rev. D75 (2007) 115017. `doi:10.1103/PhysRevD.75.115017`.

[12] M. Pospelov, Secluded U(1) below the weak scale, Phys. Rev. D80 (2009) 095002. `doi:10.1103/PhysRevD.80.095002`.

[13] O. Adriani, *et al.*, An anomalous positron abundance in cosmic rays with energies 1.5-100 GeV, Nature 458 (2009) 607–609. `doi:10.1038/nature07942`.

[14] M. Ackermann, *et al.*, Measurement of separate cosmic-ray electron and positron spectra with the Fermi Large Area Telescope, Phys. Rev. Lett. 108 (2012) 011103. `doi:10.1103/PhysRevLett.108.011103`.

[15] M. Aguilar, *et al.*, First Result from the Alpha Magnetic Spectrometer on the International Space Station: Precision Measurement of the Positron Fraction in Primary Cosmic Rays of 0.5–350 GeV, Phys. Rev. Lett. 110 (14) (2013) 141102. `doi:10.1103/PhysRevLett.110.141102`.

[16] J. D. Bjorken, R. Essig, P. Schuster, N. Toro, New Fixed-Target Experiments to Search for Dark Gauge Forces, Phys. Rev. D80 (2009) 075018. `doi:10.1103/PhysRevD.80.075018`.

[17] T. Beranek, H. Merkel, M. Vanderhaeghen, Theoretical framework to analyze searches for hidden light gauge bosons in electron scattering fixed target experiments, Phys. Rev. D88 (2013) 015032. `doi:10.1103/PhysRevD.88.015032`.

[18] K. I. Blomqvist, *et al.*, The three-spectrometer facility at the Mainz microtron MAMI, Nucl. Instrum. Methods A403 (1998) 263–301. `doi:10.1016/S0168-9002(97)01133-9`.

[19] H. Merkel, *et al.*, Search for light gauge bosons of the dark sector at the mainz microtron, Phys. Rev. Lett. 106 (2011) 251802. `doi:10.1103/PhysRevLett.106.251802`.

[20] R. Essig, P. Schuster, N. Toro, B. Wojtsekhowski, An Electron Fixed Target Experiment to Search for a New Vector Boson A' Decaying to e+e-, J. High Energy Phys. 02 (2011) 009. `doi:10.1007/JHEP02(2011)009`.

[21] B. Aubert, *et al.*, Search for Dimuon Decays of a Light Scalar Boson in Radiative Transitions $\Upsilon \rightarrow \gamma A_0$, Phys. Rev. Lett. 103 (2009) 081803. `doi:10.1103/PhysRevLett.103.081803`.

[22] S. Abrahamyan, *et al.*, Search for a New Gauge Boson in Electron-Nucleus Fixed-Target Scattering by the APEX Experiment, Phys. Rev. Lett. 107 (2011) 191804. `doi:10.1103/PhysRevLett.107.191804`.

[23] H. Merkel, P. Achenbach, C. A. Gayoso, T. Beranek, J. Bericic, *et al.*, Search for light massive gauge bosons as an explanation of the $(g-2)_\mu$ anomaly at MAMI, Phys.Rev.Lett. 112 (2014) 221802. `arXiv:1404.5502`, `doi:10.1103/PhysRevLett.112.221802`.

[24] P. Adlarson, *et al.*, Search for a dark photon in the $\pi^0 \rightarrow e^+e^-\gamma$ decay, Phys. Lett. B726 (1–3) (2013) 187 – 193. `doi:10.1016/j.physletb.2013.08.055`.

[25] D. Babusci, *et al.*, Limit on the production of a light vector gauge boson in phi meson decays with the KLOE detector, Phys. Lett. B720 (2013) 111–115. `doi:10.1016/j.physletb.2013.01.067`.

[26] G. Agakishiev, *et al.*, Searching a dark photon with HADES, Phys. Lett. B731 (2014) 265–271. `doi:10.1016/j.physletb.2014.02.035`.

[27] E. Goudzovski, Talk at "Dark Matter, Hadron Physics and Fusion Physics", Messina, to appear in EPJ Web of Conferences.

[28] J. Müller, Entwurf eines Spektrometers für Niederenergieexperimente an MESA, Diplomarbeit, Johannes Gutenberg-Universität Mainz (2014).

Search for Light Gauge Bosons of the Dark Sector at the Mainz Microtron

H. Merkel,[1,*] P. Achenbach,[1] C. Ayerbe Gayoso,[1] J. C. Bernauer,[1,†] R. Böhm,[1] D. Bosnar,[2] L. Debenjak,[3] A. Denig,[1]
M. O. Distler,[1] A. Esser,[1] H. Fonvieille,[4] I. Friščić,[2] D. G. Middleton,[1] U. Müller,[1] L. Nungesser,[1] J. Pochodzalla,[1]
M. Rohrbeck,[1] S. Sánchez Majos,[1] B. S. Schlimme,[1] M. Schoth,[1] S. Širca,[3,5] and M. Weinriefer[1]

(A1 Collaboration)

[1]*Institut für Kernphysik, Johannes Gutenberg-Universität Mainz, D-55099 Mainz, Germany*[‡]
[2]*Department of Physics, University of Zagreb, HR-10002 Zagreb, Croatia*
[3]*Jožef Stefan Institute, SI-1000 Ljubljana, Slovenia*
[4]*Clermont Université, Université Blaise Pascal, CNRS/IN2P3, LPC, BP 10448, F-63000 Clermont-Ferrand, France*
[5]*Department of Physics, University of Ljubljana, SI-1000 Ljubljana, Slovenia*

(Received 21 January 2011; published 22 June 2011)

A new exclusion limit for the electromagnetic production of a light $U(1)$ gauge boson γ' decaying to e^+e^- was determined by the A1 Collaboration at the Mainz Microtron. Such light gauge bosons appear in several extensions of the standard model and are also discussed as candidates for the interaction of dark matter with standard model matter. In electron scattering from a heavy nucleus, the existing limits for a narrow state coupling to e^+e^- were reduced by nearly an order of magnitude in the range of the lepton pair mass of $210\ \mathrm{MeV}/c^2 < m_{e^+e^-} < 300\ \mathrm{MeV}/c^2$. This experiment demonstrates the potential of high current and high resolution fixed target experiments for the search for physics beyond the standard model.

DOI: 10.1103/PhysRevLett.106.251802 PACS numbers: 14.70.Pw, 25.30.Rw, 95.35.+d

Introduction.—An additional $U(1)$ interaction appears to be natural in nearly all theoretical extensions of the standard model. Large gauge symmetries have to be broken, and $U(1)$ bosons provide the lowest-rank local symmetries. For example, in standard embedding of most variants of string theories, a $U(1)$ boson is generated by symmetry breaking. Such additional $U(1)$ bosons may be hidden; e.g., no standard model particles are charged under the corresponding symmetry, but their mass is allowed in the range of the standard model masses.

Recently, several experimental anomalies were discussed as possible signatures for a hidden force. A light $U(1)$ boson in the mass range below 1 GeV/c^2 might explain, e.g., the observed anomaly of the muon magnetic moment [1,2]. Cosmology and astrophysics provide an abundant amount of evidence for the existence of dark matter (for a summary, see, e.g., Ref. [3]). Several experimental hints point to a $U(1)$ boson coupling to leptons as the mediator of the interaction of dark matter with standard model matter (see, e.g., Ref. [4] for a detailed discussion). For example, the lively debated annual modulation signal of the DAMA-LIBRA experiment [5] could be brought into accordance with the null result of bolometric experiments if one assumes an interaction via a light $U(1)$ boson [6]. Observations of cosmic rays show a positron excess [7]. While this excess may be due to astrophysical process like quasars, this could also be a hint for the annihilation of dark matter into leptons. If the experimental evidence is interpreted as annihilation of dark matter, the excess of positrons and no excess of antiprotons in cosmic rays hints again to a mass of the $U(1)$ boson below 2 GeV/c^2.

The interaction strength of such a $U(1)$ boson (in the following denoted as γ', in the literature also denoted as A', U, or ϕ) with standard model particles is governed by the mechanism of kinetic mixing [8]. The coupling can be subsumed by an effective coupling constant ϵ and a vertex structure of a massive photon.

Bjorken *et al.* [9] discussed several possible experimental schemes for the search of a γ' in the most likely mass range of a few MeV/c^2 up to a few GeV/c^2. Since the coupling is small, the cross section for coherent electromagnetic production of the γ' boson can be enhanced by a factor Z^2 by choosing a heavy nucleus as the target (see Fig. 1). The subsequent decay of the γ' boson to a lepton pair is the signature of the reaction.

The cross sections of signal and background were estimated in Ref. [9] in the Weizsäcker-Williams approximation. In this approximation, the cross section shows a sharp

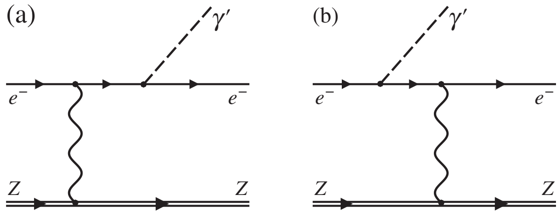

FIG. 1. Electromagnetic production of the γ' boson. The coupling of the γ' boson is parametrized as $i\epsilon e\gamma^\mu$.

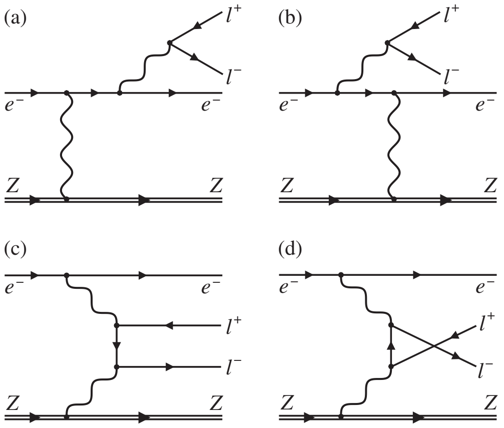

FIG. 2. Dominant background processes. While graphs (a) and (b) have the same structure as the signal and present an irreducible background, the contributions of graphs (c) and (d) can be suppressed by the choice of kinematic setting.

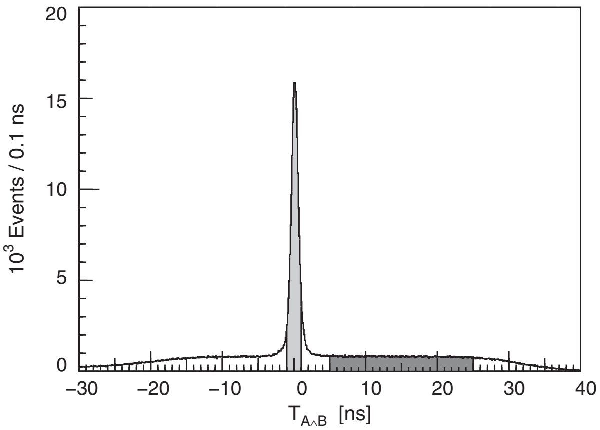

FIG. 3. Coincidence time distribution after particle identification by Čerenkov detectors (setup 1). The events of the light shaded area were used as true coincidences, while the dark shaded area was used as an estimate of the accidental coincidences.

peak, in both signal and background, where nearly all the energy of the incident electron is transferred to the lepton pair $(E_{e^+} + E_{e^-}) = E_0$. Correspondingly, the pair is produced dominantly in the direction of the incident electron.

The experimental challenge is the suppression of the background, which is dominated by radiative pair production (Fig. 2). Radiation by the final or initial electron [Figs. 2(a) and 2(b)] has the same cross-section structure as the desired signal and is an irreducible background to this experiment. Radiation with an internal lepton line [Figs. 2(c) and 2(d)] has a maximum if the internal electron line is nearly on the mass shell, i.e., if one of the leptons carries nearly all the energy of the pair. This background can be reduced by choosing a kinematic setting in which the electron and positron are detected at equal angles and momenta.

Experiment.—The experiment took place at the spectrometer setup of the A1 Collaboration at the Mainz Microtron (MAMI) (see Ref. [10] for a detailed description). An unpolarized electron beam with a beam energy of $E_0 = 855$ MeV and a beam current of 90 μA was incident on a tantalum foil (99.9% ^{181}Ta, $Z = 73$) with an area density of 81.3 mg/cm^2, leading to a luminosity of $LZ^2 = 8.07 \times 10^{38}\ \mathrm{s}^{-1}\,\mathrm{cm}^{-2}$. The beam was rastered across the target to reduce the local thermal load on the target foil.

For the detection of the electron-positron pair, two high-resolution spectrometers were used. The particles were detected by vertical drift chambers for tracking and scintillator detectors for trigger and timing purposes. In addition, a threshold-gas-Čerenkov detector was used in each arm to discriminate between electrons or positrons and pions.

Table I summarizes the kinematic setups used. Setup 1 was chosen to be close to $E_{e^+} + E_{e^-} = E_0$, where the cross section has a sharp peak to ensure high count rates. In addition, setup 2 was selected at $E_{e^+} + E_{e^-} = 0.9E_0$ during the experiment to optimize the total count rates. The angles of the spectrometers were set to be nearly symmetric to reduce the background by the Bethe-Heitler process [Figs. 2(c) and 2(d)]. In total, data of four days of beam time were used for the analysis. The electrons and the positrons were detected by the coincidence of the raw scintillator signals. The Čerenkov signals were not included in the trigger logic but recorded for off-line analysis.

Data analysis.—Only events with a positive signal in the Čerenkov detectors were selected with an efficiency of 98% for spectrometer A and 95% for spectrometer B [10]. Figure 3 shows the coincidence time between the corresponding spectrometers after correction for the flight path of ≈ 12 m within the spectrometers for these events. A timing resolution of better than 1 ns FWHM was achieved, and a cut of $-1\ \mathrm{ns} < t_{A\wedge B} < 1$ ns was used to mark the true electron-positron pairs. Below the peak, a

TABLE I. Kinematic settings. The incident beam energy was $E_0 = 855$ MeV, and the settings are roughly centered around $E_{e^+} + E_{e^-} = E_0$ and $m_{\gamma'} = 250\ \mathrm{MeV}/c^2$.

	Spec. A (e^+)			Spec. B (e^-)			
	p (MeV)	θ	$d\Omega$ (msr)	p (MeV)	θ	$d\Omega$ (msr)	Events
Setup 1	346.3	22.8°	21	507.9	15.2°	5.6	208×10^6
Setup 2	338.0	22.8°	21	469.9	15.2°	5.6	47×10^6

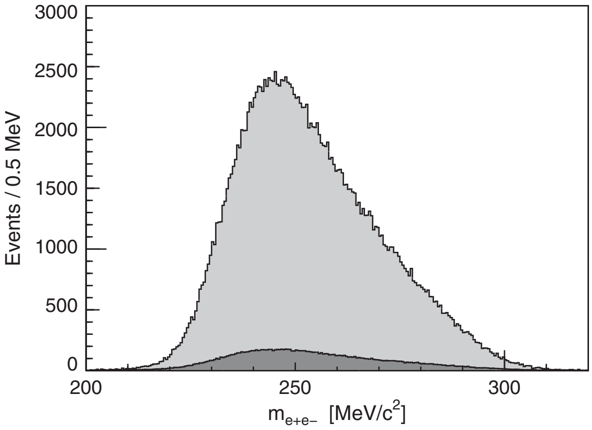

FIG. 4. Mass distribution of the reconstructed e^+-e^- pair (setup 1). The dark shaded area denotes the background due to accidental coincidences (scaled to a time window of 2 ns).

background due to accidental coincidences is present. To estimate this background, events in the coincidence side band 5 ns $< t_{\mathrm{A}\wedge\mathrm{B}} <$ 25 ns were selected and weighted by the ratio of the timing windows.

For the real electron-positron pairs, the invariant mass squared of the pair was determined by the four-momentum sum $m^2_{e^+e^-} = (p_{e^+} + p_{e^-})^2$. Figure 4 shows the resulting mass spectrum. The contribution of the accidental background is indicated by the dark shaded area.

In this figure, a possible candidate for the dark photon would appear as a peak on top of the background. The width of such a peak can only be estimated by simulation. For this, the experimental resolution of the four-vector determination of a single spectrometer was determined by the width of the lowest lines of the nuclear excitation spectrum in elastic electron scattering. This single spectrometer resolution was used as input for the simulation of the experiment. A mass resolution of better than 0.5 MeV$/c^2$ was determined, corresponding to the chosen bin width in Fig. 4.

No significant peak in the mass spectrum was observed. The corresponding upper limit was determined by the Feldman-Cousins algorithm [11]. As input for this algorithm the raw mass spectrum was used, and as a background estimate for each bin the mean of the three neighboring bins on either side was used. This choice of the background estimate introduces systematic errors, which have to be investigated in the case of a positive signal but only enhance statistical fluctuations in the case of an upper limit. Figure 5 shows the resulting exclusion limits.

Results and interpretation.—In order to interpret the result in terms of the effective coupling ϵ of a possible dark photon candidate, a model for the production process has to be used. Unfortunately, it turns out that the Weizsäcker-Williams approximation used in Ref. [9] fails in this energy range by orders of magnitude, mainly since the recoil of the nucleus cannot be neglected. Taking into account the nuclear recoil, the peak at $(E_{e^+} + E_{e^-}) = E_0$ in Ref. [9] is regularized, and the cross section at this point becomes zero. In addition, the assumption of a real initial photon exactly in the direction of the electron beam introduces a peak in the angular distribution, which is not present in electroproduction due to helicity conservation of the scattered electron.

Instead, we used as a model for the γ' production the coherent electroproduction from the tantalum nucleus, calculated as the coherent sum of the graphs of Fig. 1. The charge distribution of tantalum was approximated as a solid sphere. For the QED background we used the coherent sum of the graphs of Fig. 2. The corresponding cross sections were included on an event by event basis in the simulation. The simulation including this model shows excellent agreement with data, as demonstrated in Fig. 6, where the background-subtracted yields as an estimate for the QED background graphs are compared to the simulation of this process.

The remaining model dependence of this interpretation mainly affects the nuclear vertex, since, e.g., the possible

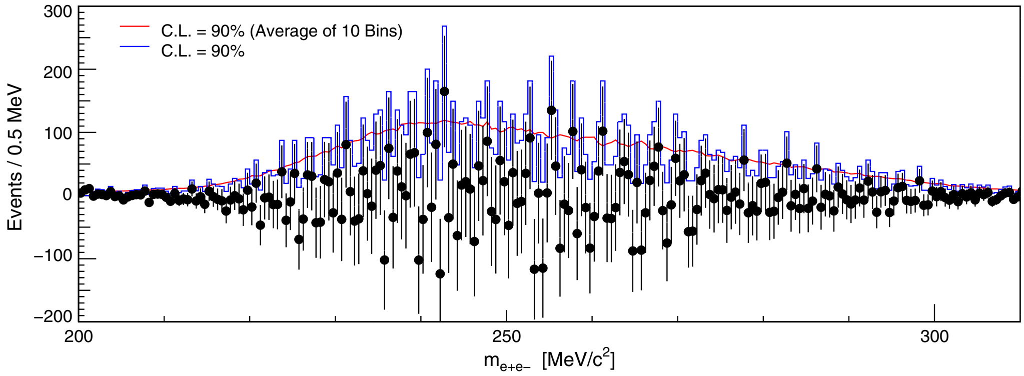

FIG. 5 (color online). Upper exclusion limits with 90% confidence level determined by the Feldman-Cousins algorithm (all data). The averaged limit is included for subjective judgement only (≈ 10% of the data points should be above this line at 90% C.L.).

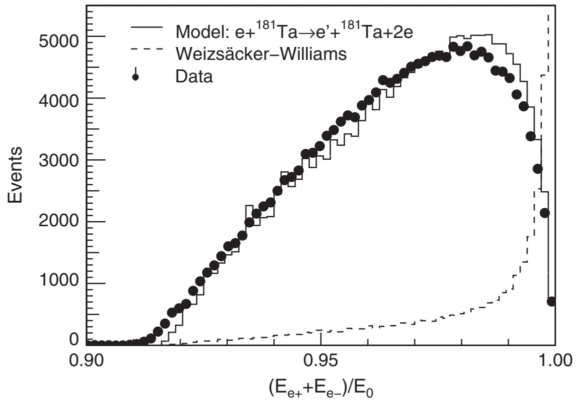

FIG. 6. Comparison of simulation with data (setup 1). As a model the coherent electroproduction from a heavy nucleus was used.

breakup of the recoil nucleus is neglected. Since this vertex is common to both the signal and the QED background channels, to further reduce the model dependence we use only the ratio of the signal to QED background of the simulation in addition to the accidental background. The ratio can be translated to the effective coupling for a given mass resolution δ_m by using Eq. (19) of Ref. [9]:

$$\frac{d\sigma(X \to \gamma' Y \to e^+e^- Y)}{d\sigma(X \to \gamma^* Y \to e^+e^- Y)} = \frac{3\pi}{2N_f}\frac{\epsilon^2}{\alpha}\frac{m_{\gamma'}}{\delta_m}$$

and the measured event rate as an estimate for the background channel. The number of final states N_f includes the ratio of phase space for the corresponding decays above the $\mu^+\mu^-$ threshold.

Figure 7 shows the result of this experiment in terms of the ratio of the effective coupling to the fine structure constant $\alpha'/\alpha = \epsilon^2$. For clarity of the figure, the exclusion limit was averaged. Also shown are the existing limits published by *BABAR* [12] and the standard model prediction [2] of the muon anomalous magnetic moment $a_\mu = g_\mu/2 - 1$ (calculation of exclusion limits in ϵ^2 by [13]). The existing exclusion limit has been extended by an order of magnitude.

In this experiment, the discovery potential of the existing high luminosity electron accelerators has been demonstrated. The background conditions are well under control due to excellent timing and missing mass resolution. An extensive program to cover further mass regions with similar experiments is planned at MAMI, Jefferson Lab [13], and other laboratories (for a review, see Ref. [14]).

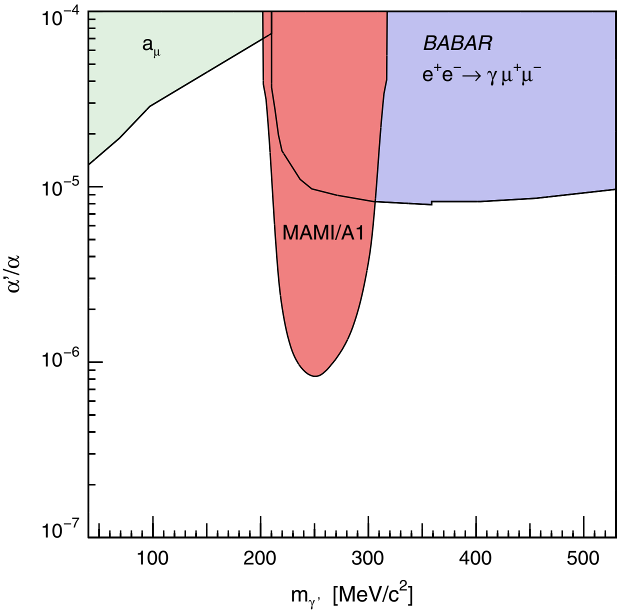

FIG. 7 (color online). Exclusion limits with 90% confidence level in terms of relative coupling $\alpha'/\alpha = \epsilon^2$. Also shown are the previous results by *BABAR* [12] and for a_μ of the muon [2].

The authors thank the MAMI accelerator group for providing the excellent beam quality and intensity necessary for this experiment and T. Beranek for fruitful discussions on the QED calculations. This work was supported by the Federal State of Rhineland-Palatinate and by the Deutsche Forschungsgemeinschaft with the Collaborative Research Center 443.

---

[*] merkel@kph.uni-mainz.de

[†] Present address: MIT-LNS, Cambridge, MA, USA.

[‡] http://www.kph.uni-mainz.de

[1] G. W. Bennett *et al.*, Phys. Rev. D **73**, 072003 (2006).
[2] M. Pospelov, Phys. Rev. D **80**, 095002 (2009).
[3] K. Nakamura *et al.* (Particle Data Group), J. Phys. G **37**, 075021 (2010).
[4] N. Arkani-Hamed, D. P. Finkbeiner, T. R. Slatyer, and N. Weiner, Phys. Rev. D **79**, 015014 (2009).
[5] R. Bernabei *et al.*, Eur. Phys. J. C **56**, 333 (2008).
[6] N. Borodatchenkova, D. Choudhury, and M. Drees, Phys. Rev. Lett. **96**, 141802 (2006).
[7] O. Adriani *et al.*, Nature (London) **458**, 607 (2009).
[8] B. Holdom, Phys. Lett. **166B**, 196 (1986).
[9] J. D. Bjorken, R. Essig, P. Schuster, and N. Toro, Phys. Rev. D **80**, 075018 (2009).
[10] K. I. Blomqvist *et al.*, Nucl. Instrum. Methods Phys. Res., Sect. A **403**, 263 (1998).
[11] G. J. Feldman and R. D. Cousins, Phys. Rev. D **57**, 3873 (1998).
[12] B. Aubert *et al.*, Phys. Rev. Lett. **103**, 081803 (2009).
[13] R. Essig, P. Schuster, N. Toro, and B. Wojtsekhowski, J. High Energy Phys. 02 (2011) 009.
[14] S. Andreas and A. Ringwald, arXiv:1008.4519.

PHYSICAL REVIEW D **88,** 015032 (2013)

Theoretical framework to analyze searches for hidden light gauge bosons in electron scattering fixed target experiments

T. Beranek, H. Merkel, and M. Vanderhaeghen

PRISMA Cluster of Excellence, Johannes Gutenberg-Universität Mainz, D-55099 Mainz, Germany
and Institut für Kernphysik, Johannes Gutenberg-Universität Mainz, D-55099 Mainz, Germany

(Received 20 March 2013; published 29 July 2013)

Motivated by anomalies in cosmic ray observations and by attempts to solve questions of the Standard Model of particle physics like the $(g-2)_\mu$ discrepancy, $U(1)$ extensions of the Standard Model have been proposed in recent years. Such $U(1)$ extensions allow for the interaction of dark matter by exchange of a photonlike massive force carrier γ' not included in the Standard Model. In order to search for γ' bosons, various experimental programs have been started. One approach is the dedicated search at fixed-target experiments at modest energies as performed at microtron (MAMI) or at the Jefferson Lab. In these experiments the process $e(A,Z) \to e(A,Z)l^+l^-$ is investigated, and a search for a very narrow resonance in the invariant mass distribution of the l^+l^- pair is performed. In this work we analyze this process in terms of signal and background in order to describe existing data obtained by the A1 experiment at MAMI with the aim to give accurate predictions for exclusion limits in the γ' parameter space. We present a detailed theoretical analysis of the cross sections entering in the description of such processes.

DOI: 10.1103/PhysRevD.88.015032 PACS numbers: 14.70.Pw, 12.60.Cn, 13.85.Rm

I. INTRODUCTION

With the recent observation of a new boson at the LHC, which is expected to be the Higgs boson, the last missing element of the Standard Model of particle physics (SM) seems to be discovered [1,2]. Despite this, nowadays the existence of dark matter, which is not included in the SM, is established as a necessary ingredient in order to explain the energy density of the Universe within the cosmological standard model [3–5]. The nature of dark matter is, however, still a wide open question. Neither is it known what dark matter is made of nor in which way it is interacting with other particles, e.g. the SM particles. Besides the unsolved problem of dark matter, the SM itself does contain several issues like the discrepancy in the theoretical and experimental determination of the anomalous magnetic moment of the muon $(g-2)_\mu$, the proton radius puzzle, or weak scale questions like the hierarchy problem, which all could be hints for physics beyond the SM.

Recent observations of anomalies in astrophysical data [6–8] have motivated one to consider extensions of the SM by including an additional $U(1)$ gauge group which could explain such anomalies [9,10]. Though the idea to extend the SM by an additional $U(1)$ recently became popular, it did not rise up with the observations. In many well motivated SM extensions, e.g. from string theory, additional $U(1)$ groups appear naturally [11–16].

Extending the SM by such a $U(1)_D$ group generates an additional gauge boson γ' which is able to interact with the electromagnetic current of the Standard Model. Although this interaction is forbidden at tree level, it is possible via kinetic mixing [13] giving rise to an effective interaction Lagrangian

$$\mathcal{L}_{\rm int} = i\varepsilon e \bar{\psi}_{\rm SM}\gamma^\mu \psi_{\rm SM} A'_\mu,$$

where A' denotes the γ' field. Furthermore, ε is the kinetic mixing factor parametrizing the coupling strength relative to the electric charge e and describes the interaction of the additional gauge boson with the electromagnetic current. The γ' may gain a mass $m_{\gamma'}$ which can be estimated to be in the range of 10 MeV to a few GeV [17–19]. The kinetic mixing factor $\varepsilon^2 = \alpha'/\alpha$ is predicted from various models to be in the range $10^{-12} < \varepsilon < 10^{-2}$ [19,20]. Due to the coupling via kinetic mixing, the γ' may decay to dark matter particles as well as SM matter particles. In the case that the decay to dark matter is kinematically forbidden and $m_{\gamma'} > 2m_e = 1.022$ MeV, which this work will focus on, the γ' will decay to SM particles and therefore must be observable at accelerator experiments.

The γ' interacts with SM particles and has properties which are very similar to that of the photon. Since by now such a boson could not be observed, one often refers to the γ' (which is also denoted as A', U, ϕ) as a heavy, hidden, para-, or dark photon. Within this minimal model, the free parameters are the mass $m_{\gamma'}$ and the coupling strength ε. In pioneering works several constraints from existing data were obtained on these parameters e.g. in beam dump searches or by the *BABAR* experiment, as well as from $(g-2)$ analyses [15,21].

The coupling of the γ' to SM particles and the predicted mass range allows for the γ' search by accelerator experiments at modest energies with high intensities. While collider experiments are ideally suited for higher γ' masses, fixed-target experiments with their high luminosities are ideally suited for the γ' search in the MeV to 1 GeV range [19,21–24]. The proposal to search for the hidden gauge boson by fixed-target experiments motivated

1550-7998/2013/88(1)/015032(14)

several experimental programs, both by the A1 Collaboration at the Mainz Microtron (MAMI) accelerator in Mainz [25] as well as at the Jefferson Lab (JLAB) with the APEX [26,27], HPS [28] and DarkLight [29,30] experiments. The A1 and APEX experiments already have published first data. Furthermore, in many recent publications, constraints on the γ' parameter space from the analysis of beam dump searches [31–34], meson decays, and collider experiments [35–39] as well as from other arguments were given [40,41] and are summarized in Fig. 12. In addition, many other experiments were proposed to probe the light hidden sector or are underway, for a review see, e.g., Ref. [42].

In all considered fixed-target experiments, an electron beam is scattered off a fixed target which is either a proton or a heavy nucleus like tantalum. Induced by this electromagnetic process, a γ' may be radiated from the electron beam and decays into SM particles like an electron-positron pair. Detecting the decay particles and reconstructing the invariant mass of the pair allows one to search for the hidden gauge boson by a bump hunt. The γ' will manifest itself by a very sharp peak above the radiative background that results from the corresponding process where a virtual photon is radiated from the electron beam which creates a lepton pair, too; i.e. the underlying process

$$e(A, Z) \rightarrow e(A, Z) l^+ l^-$$

is investigated.

If there is no bump seen in the invariant mass spectrum, this allows one to exclude regions of the γ' parameter space given by the kinetic mixing factor ε and its mass $m_{\gamma'}$. In order to perform this study, a precise knowledge of the signal and background cross sections are crucial. Such precise study is the main subject of the present work.

This work is structured as follows. In Sec. II we present our calculations of the signal and background cross sections. In Sec. III we present our results of the cross section calculations for the experiments performed at MAMI. Furthermore, we present a comparison with available data. In Sec. IV we propose new searches at MAMI and at the new Mainz Energy Recovering Accelerator (MESA) and present our predictions for the exclusion limits.

II. CALCULATION OF THE SIGNAL AND BACKGROUND CROSS SECTIONS

The underlying diagrams for all fixed-target experiments mentioned so far are shown in Fig. 1. We calculate this process exactly in leading order of QED and furthermore apply leading-order radiative corrections of the corresponding elastic scattering process to obtain an estimate of these corrections.

An electron beam of energy E_0 is scattered off a fixed target, which may either be a nucleon or a heavy nucleus of atomic numbers (A, Z). In the following, the target mass M refers to the nucleon mass M_N or to the mass of the heavy nucleus $M_A \simeq A \times M_N$. As a subprocess to the elastic scattering, an intermediate vector particle V is produced and creates a lepton pair $(l^+ l^-)$, where the lepton mass is

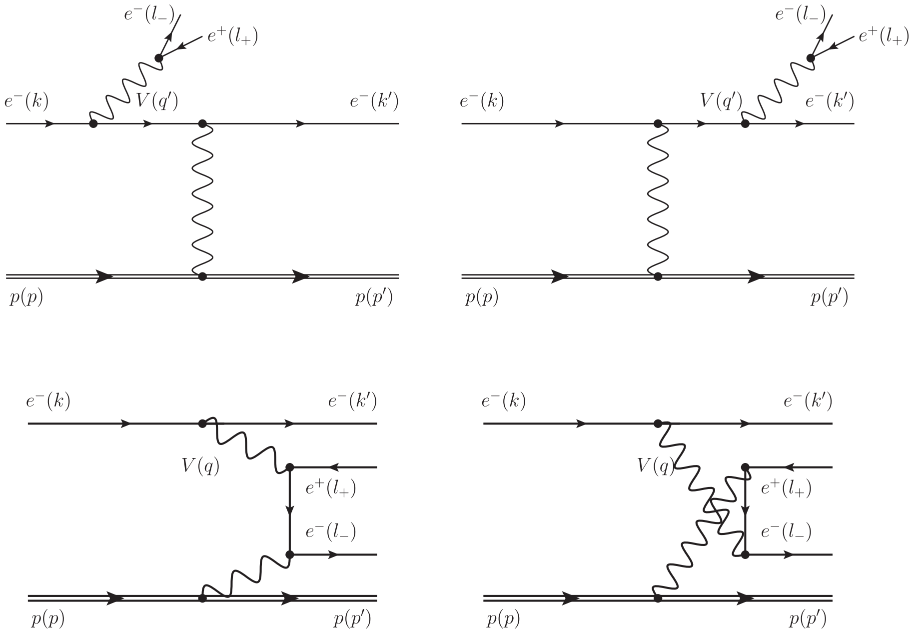

FIG. 1. Tree-level Feynman diagrams contributing to the $ep \rightarrow epl^+l^-$ amplitude. Upper panel: exchange of the timelike boson V and a spacelike γ (TL). Lower panel: the spacelike boson V and a spacelike γ (SL). In addition to these direct (D) diagrams, the exchange term (X), which consists of the same set of diagrams with scattered electron and electron of the e^+e^- pair exchanged, also contributes.

denoted by m_l. Although the existing and planned fixed-target experiments only consider electron-positron pairs in which a bump hunt is performed, our calculations are performed generally for any kind of lepton species (i.e. also applies to the $\mu^+\mu^-$ case); i.e. we do not neglect the mass of the lepton.

The isolated γ' production process is given by the coherent sum of diagrams (a) and (b) while the background, resulting from the exchange of a virtual photon, is given by the sum over all diagrams, where the intermediate vector particle V in diagrams (a) and (b) is γ' and γ^*, respectively.

We assign a finite decay width $\Gamma_{\gamma'}$ to the γ'. The partial decay width to a SM lepton pair l^+l^- is given by

$$\Gamma_{\gamma' \to l^+ l^-} = \frac{\alpha \varepsilon^2}{3 m^2_{\gamma'}} \sqrt{m^2_{\gamma'} - 4 m_l^2}(m^2_{\gamma'} + 2 m_l^2),$$

with $\alpha = e^2/(4\pi) \simeq 1/137$.

For kinematically forbidden decays to dark matter, the total width can be related to the partial width by $\Gamma_{\gamma'} = N_{\rm eff} \times \Gamma_{\gamma' \to l^+ l^-}$, where $N_{\rm eff}$ is a weight to account for other degrees of freedom in SM decays. Since in this case the width is very small, only a small mass window around the peak will contribute to the signal, and thus the cross sections for real and virtual γ' multiplied by $N_{\rm eff}$ are equal [21,29].

In this work we denote the four-momenta of the initial and final beam electrons by $k = (E_0, \vec{k})$ and $k' = (E'_e, \vec{k}')$, the four-momenta of the initial and final target state by $p = (E_p, \vec{p})$ and $p' = (E'_p, \vec{p}')$, and the lepton pair four-momenta by $l_- = (E_-, \vec{l}_-)$ and $l_+ = (E_+, \vec{l}_+)$ for the lepton and antilepton, respectively. The initial and final electron spins are denoted by s_k and s'_k, the spins of the initial and final proton by s_p and s'_p, and the spins of the created lepton and antilepton by s_- and s_+. Furthermore, we follow the conventions of Bjorken and Drell [43].

The invariant amplitudes required to calculate the cross section can be read of from these Feynman diagrams. As in the two diagrams in the upper panel of Fig. 1, the intermediate boson V is timelike; we refer to this amplitude as TL. Correspondingly, we refer to the diagrams in the lower panel, where the V is spacelike, as SL, and their sum is denoted by SL + TL.

In the case that the l^+l^- pair and the beam lepton are of the same species as for the existing experiments, another set of diagrams is allowed. Since one cannot distinguish the electrons in the final state, the same diagrams of Fig. 1 with the scattered (beam) electron and created electron of the pair exchanged also have to be taken into account. Therefore, following the notation of Ref. [43], we refer to the diagrams depicted in Fig. 1 as "direct" contribution and to those with exchanged final state electrons as "exchange" contribution, labeled by D and X, respectively.

For the TL diagrams, one finds for the isolated γ' production process

$$\mathcal{M}^{\rm TL}_{\gamma'} = \frac{i e^4 \varepsilon^2}{(p'-p)^2} \frac{-g^{\alpha\beta} + q'^{\alpha} q'^{\beta}/m^2_{\gamma'}}{q'^2 - m^2_{\gamma'} + i m_{\gamma'} \Gamma_{\gamma'}} J^{\mu}_N \mathcal{I}_{\mu\alpha} j^{\rm pair}_{\beta}, \qquad (1)$$

where $\Gamma_{\gamma'}$ denotes the total γ' decay width. The amplitude of the γ^* background is given by

$$\mathcal{M}^{\rm TL}_{\gamma^*} = \frac{i e^4}{(p'-p)^2} \frac{-g^{\alpha\beta}}{q'^2} J^{\mu}_N \mathcal{I}_{\mu\alpha} j^{\rm pair}_{\beta}, \qquad (2)$$

where the external momenta are denoted by $q = k - k'$, $q' = l_+ + l_-$ as in Fig. 1. Furthermore, the leptonic tensors are given by

$$\begin{aligned} \mathcal{I}_{\mu\alpha} &= \bar{u}_e(k', s'_k) \bigg(\gamma_\mu \frac{(\gamma \cdot (k - q')) + m}{(k - q')^2 - m^2} \gamma_\alpha \\ &\quad + \gamma_\alpha \frac{(\gamma \cdot (k' + q')) + m}{(k' + q')^2 - m^2} \gamma_\mu \bigg) u_e(k, s_k), \\ j^{\rm pair}_{\beta} &= \bar{u}_l(l_-, s_-) \gamma_\beta v_l(l_+, s_+), \end{aligned}$$

with m denoting the mass of the electron. While in the case of a proton target, the hadronic current J^μ_N is given by

$$J^\mu_N = \bar{u}_N(p', s'_p) \Gamma^\mu u_N(p, s_p),$$

with the parametrization of $\Gamma_\mu(Q_t^2) \equiv F_1(Q_t^2)\gamma_\mu + F_2(Q_t^2) i\sigma_{\mu\nu} q_t^\nu / 2M$ using the Dirac and Pauli form factors F_1 and F_2 and $Q_t^2 = -(p - p')^2 > 0$. For a heavy nucleus, it can be written to good approximation as

$$J^\mu_N = Z \cdot F(Q_t) \cdot (p + p')^\mu,$$

where $F(Q_t) = 3/(Q_t R)^3 \cdot (\sin(Q_t R) - Q_t R \cos(Q_t R))$ is the nuclear charge form factor with $R = 1.21\ \mathrm{fm} \cdot A^{\frac{1}{3}}$ [44]. The nucleus spin as well as contributions from the breakup channel and nuclear excitations can be neglected to good approximation. Effects due to the nucleus spin are suppressed by the large nucleus mass, which can be checked analytically. In the considered range of momentum transfer onto the hadron, the inelastic contribution can be neglected since the momenta transferred to the nucleus are small and the elastic contribution is dominant. From comparison with Eqs. (A18) and (A19) of Ref. [21], we estimate the uncertainty from this approximation entering in the calculation of the integrated cross section around 5%.

The numerator of the γ' propagator in Eq. (1) can be simplified as $(-g^{\alpha\beta})$ since the four-momentum q' is contracted with the lepton current $j^{\rm pair}$, and thus the second term vanishes due to current conservation.

For the SL diagrams, the invariant amplitude is given by

$$\mathcal{M}^{\rm SL}_{\gamma^*} = \frac{i e^4}{(p'-p)^2} \frac{-g^{\alpha\beta}}{q^2} J^{\mu}_N \tilde{\mathcal{I}}_{\mu\alpha} j^{\rm beam}_{\beta}, \qquad (3)$$

with

$$\tilde{\mathcal{I}}_{\mu\alpha} = \bar{u}_l(l_-, s_-)\Big(\gamma_\mu \frac{(\gamma\cdot(q-l_+))+m_l}{(q-l_+)^2-m_l^2}\gamma_\alpha + \gamma_\alpha \frac{(\gamma\cdot(l_- - q))+m_l}{(l_- - q)^2-m_l^2}\gamma_\mu\Big)v_l(l_+, s_+),$$

$$j_\beta^{\text{beam}} = \bar{u}_e(k', s'_k)\gamma_\beta u_e(k, s_k).$$

Although the virtual γ' exchange via the SL process is not forbidden, it will not be considered here as it would not result in any bump in the e^+e^- mass spectrum. The propagator in Eq. (3) in that case would be replaced by

$$\frac{-g^{\alpha\beta}}{q^2} \rightarrow \frac{-g^{\alpha\beta}}{q^2 - m_{\gamma'}^2},$$

and due to the spacelike $q^2 < 0$ for scattering processes, the denominator always leads to a suppression of this contribution, whereas the denominator in Eq. (1) leads to a peak in the signal. Thus, this contribution of virtual γ' exchange via the SL process to the cross section can be neglected.

In the case of a proton target, another important contribution, the double virtual Compton scattering (VCS), emerging from the third set of Feynman diagrams shown in Fig. 2, appears. In the case of a heavy nucleus target, this term is strongly suppressed due to the large mass. In this work we will restrict our study to estimate the influence of the nucleon pole contribution drawn in Fig. 2 which serves as a good approximation. The invariant amplitude is given by

$$\mathcal{M}_{\gamma'}^{\text{VCS}} = \frac{-ie^4\varepsilon^2}{q^2}\frac{-g^{\alpha\beta} + q'^\alpha q'^\beta/m_{\gamma'}^2}{q'^2 - m_{\gamma'}^2 + im_{\gamma'}\Gamma_{\gamma'}} j_{\text{beam}}^\mu \mathcal{H}_{\mu\alpha} j_\beta^{\text{pair}}, \tag{4}$$

for the isolated γ' production process and

$$\mathcal{M}_{\gamma^*}^{\text{VCS}} = \frac{-ie^4}{q^2}\frac{-g^{\alpha\beta}}{q'^2} j_{\text{beam}}^\mu \mathcal{H}_{\mu\alpha} j_\beta^{\text{pair}} \tag{5}$$

for the γ^* background, with

$$\mathcal{H}_{\mu\alpha} = \bar{u}_p(p', s'_p)\Big(\Gamma_\mu(q_t+q')\frac{(\gamma\cdot(p-q'))+M_N}{(p-q')^2-M_N^2}\Gamma_\alpha(-q') + \Gamma_\alpha(-q')\frac{(\gamma\cdot(p'+q'))+M_N}{(p'+q')^2-M_N^2}\Gamma_\mu(q_t+q')\Big) \times u_p(p, s_p).$$

As mentioned before, the electron from the scattered beam and the one from the lepton pair cannot be distinguished, and besides the direct term the exchange term has to be accounted for. Therefore, the full amplitude of the process reads as

$$\begin{aligned}\mathcal{M}_{\gamma'+\gamma^*} &= (\mathcal{M}_{\gamma'}^{\text{TL}} + \mathcal{M}_{\gamma^*}^{\text{TL}} + \mathcal{M}_{\gamma^*}^{\text{SL}}) \\ &\quad - ((\mathcal{M}_{\gamma'}^{\text{TL}} + \mathcal{M}_{\gamma^*}^{\text{TL}} + \mathcal{M}_{\gamma^*}^{\text{SL}})(e^- \leftrightarrow l^-)) \\ &= (\mathcal{M}_{\text{D},\gamma'}^{\text{TL}} + \mathcal{M}_{\text{D},\gamma^*}^{\text{TL}} + \mathcal{M}_{\text{D},\gamma^*}^{\text{SL}}) \\ &\quad - (\mathcal{M}_{\text{X},\gamma'}^{\text{TL}} + \mathcal{M}_{\text{X},\gamma^*}^{\text{TL}} + \mathcal{M}_{\text{X},\gamma^*}^{\text{SL}}),\end{aligned} \tag{6}$$

for a heavy nucleus target and

$$\begin{aligned}\mathcal{M}_{\gamma'+\gamma^*} &= (\mathcal{M}_{\text{D},\gamma'}^{\text{TL}} + \mathcal{M}_{\text{D},\gamma^*}^{\text{TL}} + \mathcal{M}_{\text{D},\gamma^*}^{\text{SL}} + \mathcal{M}_{\text{D},\gamma^*}^{\text{VCS}}) \\ &\quad - (\mathcal{M}_{\text{X},\gamma'}^{\text{TL}} + \mathcal{M}_{\text{X},\gamma^*}^{\text{TL}} + \mathcal{M}_{\text{X},\gamma^*}^{\text{SL}} + \mathcal{M}_{\text{X},\gamma^*}^{\text{VCS}})\end{aligned}$$

for a proton target. In the second term of Eq. (6), all quantities associated with the scattered electron and the pair electron are exchanged. The exchange γ' term can be neglected, as the γ' propagator does not peak, and thus a possible signal is suppressed by ε^2. Due to the exchange of final state electron momenta, the amplitude describing the signal $\mathcal{M}_{\text{D},\gamma'}^{\text{TL}}$ as well as the background contributions $\mathcal{M}_{\text{D},\gamma^*}^{\text{TL}}$ and $\mathcal{M}_{\text{X},\gamma^*}^{\text{SL}}$ contain a structure,

$$\frac{(\gamma\cdot(k - l_- - l_+)) + m}{(k - l_- - l_+)^2 - m^2},$$

that contributes to the irreducible background. This leads to a large contribution from $\mathcal{M}_{\text{X},\gamma^*}^{\text{SL}}$ in the case of forward γ' production, since the denominator of the propagator is close to zero. Forward γ' production was proposed to enhance the signal strength, while not increasing the background $\mathcal{M}_{\gamma^*}^{\text{SL}}$. Taking the background contribution $\mathcal{M}_{\text{X},\gamma^*}^{\text{SL}}$

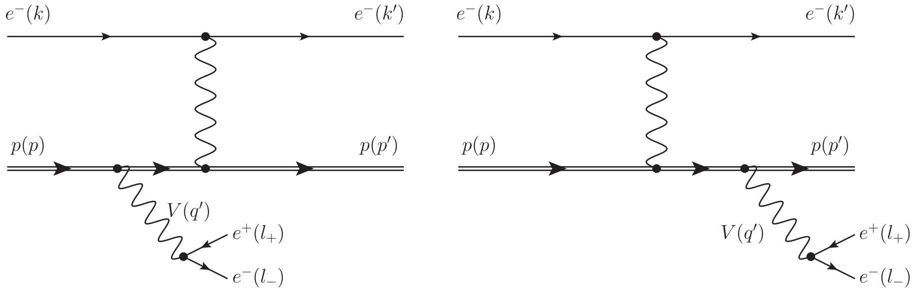

FIG. 2. Tree-level Feynman diagrams of the double VCS contribution.

into account, this argument is not applicable anymore since now the background is also enhanced.

The cross section of the $ep \to epe^+e^-$ process is computed from the general expression for $2 \to 4$ particle processes:

$$d\sigma = \frac{1}{4\sqrt{(k\cdot p)^2 - m^2M^2}}(2\pi)^4\delta^{(4)}(k+p-k'-p'-l_- - l_+) \times \frac{d^3\vec{k}'}{(2\pi)^3 2E'_e}\frac{d^3\vec{p}'}{(2\pi)^3 2E'_p}\frac{d^3\vec{l}_-}{(2\pi)^3 2E_-}\frac{d^3\vec{l}_+}{(2\pi)^3 2E_+}\overline{|\mathcal{M}|^2}. \tag{7}$$

Using a convenient set of variables, we can express the cross sections as

$$\frac{d\sigma}{dm_{ll}dE^L_{e'}d\Omega^L_{e'}d|\vec{q}'|^* d\Omega^*_{q'}d\Omega^{**}_+} = \frac{|\vec{k}'|^L}{128|\vec{k}|^L M}\frac{1}{(2\pi)^8}\frac{\lambda^{\frac{1}{2}}(s, M^2, m^2_{ll})\sqrt{m^2_{ll} - 4m^2_l}}{2s}\overline{|\mathcal{M}|^2}, \tag{8}$$

where $m_{ll} = \sqrt{q'^2}$ is the invariant mass of the l^+l^- pair, $s = (p+q)^2$ is the Mandelstam invariant of the γ^*-target subprocess, and $\lambda(s, M^2, m^2_{ll}) = (s - (M + m_{ll})^2) \times (s - (M - m_{ll})^2)$ denotes the kinematical triangle function. Furthermore, we use the superscripts L to label the lab frame, $*$ for the $(q+p)$ rest frame, and $**$ for the q' rest frame. This approach avoids ambiguities in the kinematics and automatically gives the full kinematically allowed region of the phase space. In the considered type of experiments, only a small fraction of the kinematically allowed phase space is probed. The allowed region is given by the detector acceptances in the lab frame. Therefore, it is convenient to calculate the cross section directly in terms of lab frame quantities and to use the recursively built up phase space as a cross-check.

Since fixed-target experiments are considered here, the target four-momentum p simplifies to $p = (M, \vec{0})$. Furthermore, in the considered experiments, the detectors and the beam are aligned in the same plane which we account for by the choice of our parametrization of the momentum vectors of the detected particles. Since neither the scattered hadron nor the scattered electron will be detected in the experiments, as long as the electrons are treated as distinguishable particles, the dependence of the cross section on their four-momenta has to be eliminated. Therefore, the three-momentum conserving δ function is used to eliminate the three-momentum of the final hadron state $\vec{p}'$, and energy conservation is used to express the absolute value of the three-momentum of the scattered electron $|\vec{k}'|$. The remaining dependence of the cross section on the electron scattering angle is removed by integration over the full solid angle $\Omega_{e'}$. Furthermore, one is interested in the cross section as function of the invariant mass of the created lepton pair, which is equal to the squared four-momentum of the intermediate vector boson $q'^2 = m^2_{ll}$. Therefore, we trade the absolute value of $\vec{l}_-$ for q'^2.

Thus, one finds from Eq. (7) for the differential cross section in the lab frame

$$\frac{d\sigma}{d|\vec{l}_+|d\Omega_+ d\Omega_- d\Omega_{e'} dq'^2} = \frac{1}{128|\vec{k}|M}\frac{1}{(2\pi)^8}\frac{|\vec{k}'|^2|\vec{l}_+|^2|\vec{l}_-|^2}{E_{p'}E_{k'}E_{A'}E_+E_-}\left(\left|\frac{\partial\delta_1}{\partial|\vec{k}'|}\right|\left|\frac{\partial\delta_2}{\partial|\vec{l}_-|}\right|\right)^{-1} \times\overline{|\mathcal{M}|^2}, \tag{9}$$

where this equation is understood to be evaluated with $|\vec{l}_+|$ and $|\vec{k}'|$ given in Eqs. (A5) and (A6), and $\frac{\partial\delta_1}{\partial|\vec{k}'|}$ and $\frac{\partial\delta_2}{\partial|\vec{l}_-|}$ are given by Eqs. (A7) and (A8), respectively. A more detailed derivation of the cross section is presented in the Appendix.

Furthermore, we will apply radiative corrections of elastic electron-proton scattering to the cross section to achieve a better comparability with the experimental data. Therefore, the cross section of Eq. (9) is multiplied by Eq. (A71) of Ref. [45]. By applying these radiative corrections, the value of the cross section is reduced by an amount in the range of 10%–20%.

The comparison with experimental data can be performed by integrating Eq. (9) over the experimental acceptances. To obtain the acceptance integrated cross section $\Delta\sigma$, which can be related to experimental count rates by multiplication with the luminosity, a nontrivial 8-fold integration is necessary. Furthermore, the structure of the squared matrix element contains several strongly peaked structures which makes the numerical calculation of this integral challenging. Any of the fermion and photon propagators in the Feynman diagrams shown in Fig. 1 can possibly be near the mass shell in a certain kinematical setting. Although there is no real divergence existing, since the nonvanishing mass of the electron serves as a regulator, the calculation of these strongly peaked structures either needs further approximations or a large numerical effort. In our study we try to use as few approximations as possible. We thus decide to use an integration method that allows us to deal with these peaked structures by increasing the numerical precision. Therefore, for the numerical integration, the VEGAS algorithm [46] has been chosen, which is a well established Monte Carlo integration method in particle physics. The standard deviation and the χ^2 of the result of the integration are used to decide whether the computed value is reasonable or not. During our calculations, it turned out, that—at least for the case of MAMI kinematics—one cannot use a vanishing electron mass to achieve numerically stable results. In order to perform these calculations in a reasonable amount of time, we have performed a highly parallelized calculation. Therefore, the integral is computed on graphics processing units (GPUs) using the NVIDIA CUDA framework [47] and the implementation of the

VEGAS algorithms on GPUs published in Ref. [48]. The use of the GPU version reduces the time needed for the evaluation of the acceptance integrated cross section by a factor of ∼60. We have checked the results achieved by the GPU calculation with ordinary calculations on CPUs and find that for a same numerical precision the results are equal within their standard deviations, which are below 10^{-4} relative to the obtained value.

The radiative background is described by the acceptance integrated cross section

$$\Delta\sigma_\gamma \propto |(\mathcal{M}^{\mathrm{TL}}_{\gamma^*} + \mathcal{M}^{\mathrm{SL}}_{\gamma^*}) - ((\mathcal{M}^{\mathrm{TL}}_{\gamma^*} + \mathcal{M}^{\mathrm{SL}}_{\gamma^*})(e^- \leftrightarrow l^-))|^2, \tag{10}$$

where the prefactors on the right-hand side are the same as appearing in Eq. (9). For later use, besides the cross section of the process including γ^* and γ', we define the direct timelike radiative background cross section and the direct timelike γ' cross section as

$$\Delta\sigma_{\gamma'+\gamma} \propto |\mathcal{M}^{\mathrm{TL}}_{\mathrm{D+X},\gamma'} + \mathcal{M}^{\mathrm{TL}}_{\mathrm{D+X},\gamma^*} + \mathcal{M}^{\mathrm{SL}}_{\mathrm{D+X},\Delta\gamma^*}|^2, \tag{11}$$

$$\Delta\sigma^{\mathrm{TL}}_\gamma \propto |\mathcal{M}^{\mathrm{TL}}_{\mathrm{D},\gamma^*}|^2, \tag{12}$$

$$\Delta\sigma_{\gamma'} \propto |\mathcal{M}^{\mathrm{TL}}_{\mathrm{D},\gamma'}|^2, \tag{13}$$

respectively.

In order to compute exclusion limits on the coupling strength ε from existing data, a relation between the cross sections of Eqs. (10) and (13) giving rise to ε is required. We split the $\gamma' + \gamma$ cross section as

$$\Delta\sigma_{\gamma'+\gamma} = \Delta\sigma_\gamma + \Delta\sigma_{\gamma'} + \Delta\sigma_{\mathrm{int}},$$

with $\Delta\sigma_{\mathrm{int}}$ denoting the interference part. Dividing Eq. (11) by Eq. (10) leads to

$$\frac{\Delta\sigma_{\gamma'+\gamma}}{\Delta\sigma_\gamma} = 1 + \frac{3\pi}{2N}\frac{\varepsilon^2}{\alpha}\frac{m_{\gamma'}}{\delta m}\frac{\Delta\sigma^{\mathrm{TL}}_\gamma}{\Delta\sigma_\gamma} + \frac{\Delta\sigma_{\mathrm{int}}}{\Delta\sigma_\gamma}.$$

We have used Eq. (19) of Ref. [21] in order to approximate the ratio of $\sigma_{\gamma'}$ and $\sigma^{\mathrm{TL}}_\gamma$ as

$$\frac{\Delta\sigma_{\gamma'}}{\Delta\sigma^{\mathrm{TL}}_\gamma} = \frac{3\pi}{2N}\frac{\varepsilon^2}{\alpha}\frac{m_{\gamma'}}{\delta m},$$

where N is the ratio of the decay widths $\Gamma_{\gamma'\to e^+e^-}$ and $\Gamma_{\gamma'\to\mu^+\mu^-}$ taking other possible final states into account and δm is the experimental mass resolution, i.e. the width of bin containing nearly all events of a possible signal. The formula is of course only an approximation since the data analysis of such an experiment involves a detailed simulation of the peak form and more elaborate peak search algorithms, which is beyond the scope of this paper. For γ' masses $\gtrsim 400$ MeV hadrons also contribute to the final state, and thus our parametrization of N is not valid anymore. In the γ' mass range considered in this work, only electrons and muons are contributing as possible final states. Our numerical calculations for a wide range of parameters $m_{\gamma'}$ and ε of the interference part σ_{int} from the cross sections (10), (11), and (13) show that the interference between the γ' signal and QED background can be neglected. We find that $\Delta\sigma_{\mathrm{int}}/\Delta\sigma_\gamma$ is less than 10^{-3}, which is in the range of the achieved numerical precision. Furthermore, we find a very good agreement of the approximated $\sigma_{\gamma'}/\sigma^{\mathrm{TL}}_\gamma$ with our exact calculation for the largest part of the parameter region for $m_{\gamma'}$ and ε. Therefore, ε can be computed from the cross section ratio as

$$\varepsilon^2 = \left(\frac{\Delta\sigma_{\gamma'+\gamma}}{\Delta\sigma_\gamma} - 1\right)\frac{\Delta\sigma_\gamma}{\Delta\sigma^{\mathrm{TL}}_\gamma}\frac{2N\alpha}{3\pi}\frac{\delta m}{m_{\gamma'}}.$$

The ratio $\Delta\sigma_{\gamma'+\gamma}/\Delta\sigma_\gamma$ is the (aimed) signal sensitivity, which has to be determined from the experiment. Furthermore, by using the ratio $\Delta\sigma_{\gamma'+\gamma}/\Delta\sigma_\gamma$ for the extraction of ε^2, possible effects not accounted for in our approximation of the nuclear current will cancel each other. For the prediction of exclusion limits, we estimate $\Delta\sigma_{\gamma'+\gamma}/\Delta\sigma_\gamma - 1$ as signal over background ratio

$$\frac{\sqrt{\#S}}{\#B} = \frac{2}{\sqrt{\Delta\sigma_\gamma \times L}},$$

where $\#S$ and $\#B$ are the numbers of signal and background events in one mass bin, respectively, and L is the integrated luminosity. The factor 2 results from the fact that in agreement with other publications we determine the exclusion limits on the 2σ level. Since the exclusion limit on the coupling strength ε^2 is depending linearly on the ratio of the background cross section $\Delta\sigma_\gamma$ to the TL cross section with distinguishable final state electrons $\Delta\sigma^{\mathrm{TL}}_\gamma$, the precise knowledge of these quantities is crucial to obtain an accurate result. Therefore, the next section will deal with the analysis of these background ratios for the existing experiments.

III. COMPARISON OF EXPERIMENTAL DATA AND THEORY CALCULATIONS FOR MAMI

Two dedicated fixed-target experiments, one by the A1 Collaboration at MAMI [25] and the APEX experiment at JLAB [27], have already started taking data.

A. Test run 2010

A first test run to prove the feasibility of a dedicated γ' fixed target search experiment was performed at MAMI by the A1 Collaboration in 2010 [25]. In this experiment no evidence for the existence of the γ' could be found, and an exclusion limit on the γ' parameter space was formulated. A sample of the data taken in this experiment compared to our calculations can be seen in Fig. 3.

The kinematical settings of this experiment can be taken from Table I in Ref. [25]. For the comparison of the calculation and the data, setup 1 as given in Ref. [25] was chosen, since for this setup a luminosity measurement

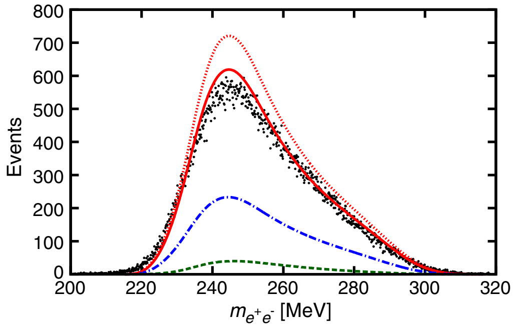

FIG. 3 (color online). Comparison of theory calculations and experimental data for a $m_{e^+e^-}$ bin width of 0.125 MeV. Black points: Data taken in a particular run of the MAMI 2010 experiment [25] in setup 1. Solid curve: Theory calculation of the background cross section. Dotted curve: Theory calculation of the background cross section without radiative corrections. Dashed-dotted curve: Theory calculation of the direct SL + TL cross section. Dashed curve: Theory calculation of the direct TL cross section.

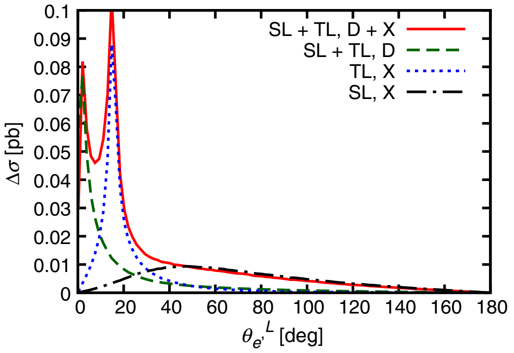

FIG. 4 (color online). Angular distribution per 0.5° with respect to the polar angle of the scattered electron for the MAMI 2010 experiment.

has been performed, finding an integrated luminosity of $\mathcal{L} = 41.4\ \mathrm{fb}^{-1}$ for the selected sample of events. A background contribution of around 5% was already subtracted in this sample; the systematic uncertainty in the luminosity from the knowledge of the thickness of the target foil is below 5%. The acceptances as shown in Table I have been used as integration limits for the theory calculation. Unless mentioned otherwise, the m_{ll} integration is performed over a range of 0.5 MeV, which is equal to the typical FWHM mass resolution of the considered experiments. As seen on Fig. 3, our calculation (solid curve) of the radiative background given by Eq. (10) and the experimental data (points) are in good agreement. Due to our estimate of the nuclear current and of the radiative corrections, we expect the small discrepancy between theory and data seen from Fig. 3. The influence of the radiative corrections is displayed by the solid and dotted curves on Fig. 3 which are calculated with and without radiative corrections, respectively. It is obvious from Fig. 3 that the applied radiative corrections lower the result of the theory calculation by an amount in the range of 10%–20%, as mentioned in Sec. II. The calculation of the full QED radiative corrections for such a process is very involved. However, one can see from Fig. 3 that our approximate treatment of the radiative corrections already provides a very good approximation, as theory and data already are in good agreement. The dashed (dashed-dotted) curve shows the direct TL (SL + TL) cross section. This indicates, that a large contribution to the cross section results from the antisymmetrization due to the indistinguishability of the scattered beam electron and the pair electron. The kinematical setting has been optimized to reduce the SL background.

TABLE I. Acceptances of the used spectrometers A and B at MAMI [49].

	Momentum	Horizontal angle	Vertical angle
A	±10%	±75 mrad	±70 mrad
B	±7.5%	±20 mrad	±70 mrad

The angular distribution with respect to the polar angle of the scattered electron presented in Fig. 4 points out that for the 2010 A1 experiment the crossed TL amplitude is responsible for a second peak in the background cross section compared to the direct amplitude (dashed curve) which only peaks at very forward scattering followed by a rapidly dropping tail. The exchange SL term nevertheless enhances the tail of the angular distribution significantly.

Figure 5 reveals that in the chosen kinematic setting, the exchange term contribution is about twice as large as the direct SL part, which initially should be minimized. This means that the largest contribution to the radiative background does not originate as assumed from the processes given by the direct SL Feynman diagrams of Fig. 1 but from the processes described by diagrams with exchanged final state electrons.

For the investigated kinematic setting, we calculate the ratio of the background cross section to the direct TL cross section which is the crucial quantity entering the determination of the exclusion limit on ε^2, according to Eq. (14). One notices from Fig. 6 (solid curve) that the ratio $\Delta\sigma_{\gamma,\mathrm{D+X}}/\Delta\sigma_{\gamma}^{\mathrm{TL}}$ smoothly varies between 15 and 25 for most of the invariant mass range. Neglecting the necessary contribution of the exchange term to the cross section, the ratio is lower by a factor of about 3 for the investigated range (dashed curve on Fig. 6).

B. 2012

The A1 Collaboration started a γ' search run at MAMI in 2012, probing the kinematics given in Table II, in which no signal of a γ' was found. The obtained invariant mass distributions can be seen in Fig. 7. The invariant mass distributions calculated from the different cross sections

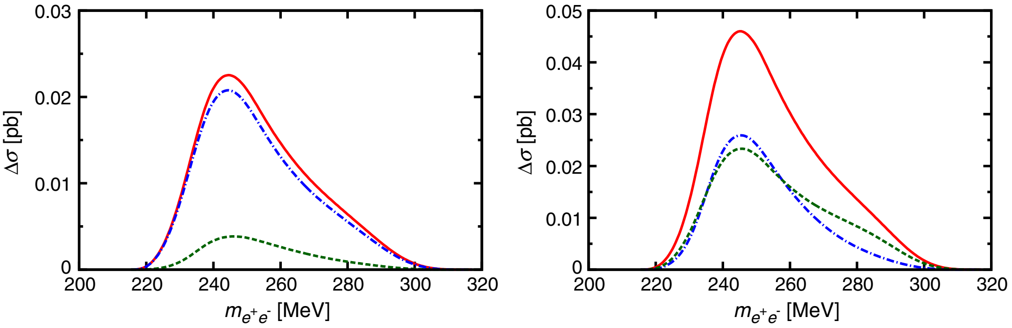

FIG. 5 (color online). Calculated direct (left panel) and exchange (right panel) term of the cross section assuming distinguishable electrons in the final state. Solid curve: SL + TL cross section. Dashed curve: TL. Dashed-dotted curve: SL.

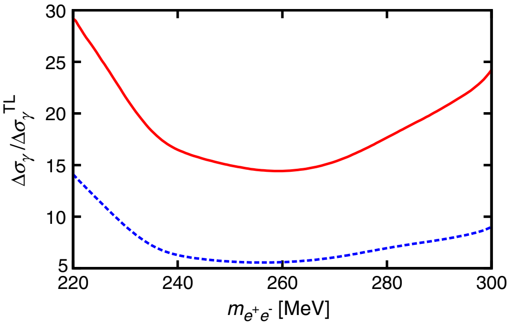

FIG. 6 (color online). Solid (dashed) curve: Ratio of the background cross section $\Delta\sigma_{\gamma,\text{D+X}}$ ($\Delta\sigma_{\gamma,\text{D}}$) to the direct TL cross section $\Delta\sigma_\gamma^{\text{TL}}$.

are compared: background (solid curve), SL + TL exchange term (dotted), SL exchange term (double-dashed), SL + TL direct term (dashed), and TL direct term (dashed-dotted). It turns out that the SL exchange process is the largest contribution to the radiative background. Figure 7 illustrates the dependence of the separated background contributions on the invariant mass $m_{e^+e^-}$. At low invariant masses, the SL exchange term dominates the cross section. Although the SL direct and the TL exchange terms become more important for increasing $m_{e^+e^-}$, the SL exchange term remains the largest contribution to the cross section. The ratio between the TL direct term and the SL exchange term has a similar behavior, retaining nearly the same maximum value in each of the considered settings. Furthermore, Fig. 7 shows the importance of the interference parts of the cross section, which are necessary to describe the data correctly.

In Fig. 8 we present a combined plot of our result for the ratio $\Delta\sigma_\gamma/\Delta\sigma_\gamma^{\text{TL}}$ for each setting given in Table II, which is crucial to obtain the exclusion limits on the γ' mass $m_{\gamma'}$ and its coupling strength ε^2 following Eq. (14), as a function of the invariant mass $m_{e^+e^-}$. Due to the particular choice of kinematics in that experiment, the ratio $\Delta\sigma_\gamma/\Delta\sigma_\gamma^{\text{TL}}$ has a value between 10–15 in the probed mass range.

In Fig. 12 our predictions for the exclusion limits on ε^2 for this set of kinematics are indicated by the dashed curve for an assumed integrated luminosity of around 10 fb^{-1}.

IV. FUTURE SEARCHES AND DISCUSSION

Recently the construction of MESA has been approved. MESA is aimed to provide a high intensity electron beam up to beam energies of about 160 MeV and thus should be ideally suited to probe the γ' parameter space for low masses. In this section we perform a feasibility study to carry out this search by using two small spectrometers.

We assume that each of these spectrometers has a horizontal and vertical angular acceptance of ±50 mrad and a momentum acceptance of ±5%. A possible γ' experiment at MESA can be performed using a gas target to minimize the multiple scattering in the target material. Therefore, applying the same program code as in Sec. III, we perform our calculations using a Xenon target in order to obtain as large cross sections as possible. The integration over the invariant mass $m_{e^+e^-}$ is performed for a 0.125 MeV interval.

The results for the obtained invariant mass distributions of this study are shown on Fig. 9. The kinematics were chosen such that the central scattering ϕ of the e^- (e^+) is $+10°$ ($-10°$), and the central momentum is $|\vec{l}|_\pm = 0.98 \times E_0/2$ for beam energies E_0 of 20, 40, 80, 120, and 160 MeV. Furthermore, we have calculated one setting for $E_0 = 120$ MeV and $\phi_\mp = \pm 20°$ in order to cover the full so-called $(g-2)_\mu$ welcome band together with the MAMI 2012 settings. We assume a beam time of about 3 months and a luminosity of 10^{34} $\text{cm}^{-2}\,\text{s}^{-1}$.

Since the low mass region $m_{\gamma'} \lesssim 10$ MeV in the $(g-2)_\mu$ discrepancy is already excluded by the electron anomalous magnetic moment $(g-2)_e$, the settings for beam energies of 20 and 40 MeV will not enter the exclusion limit calculation. Therefore, we do not have to deal with the difficulties in the low mass regime. From our exact calculation of the signal cross section $\Delta\sigma_{\gamma'}$, we find for the

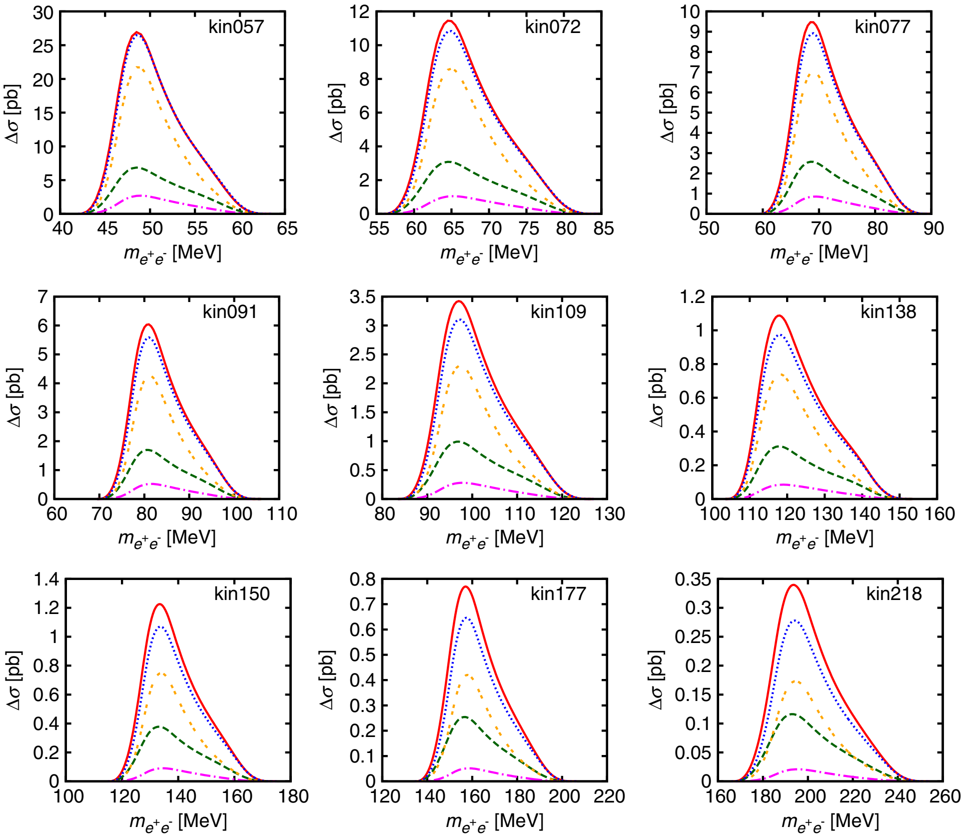

FIG. 7 (color online). Simulation of the invariant mass distributions calculated from the different cross sections for the kinematics probed at MAMI in 2012: background (solid curve), SL + TL exchange term (dotted), SL exchange term (double-dashed), SL + TL direct term (dashed), and TL direct term (dashed-dotted).

considered range of parameters a good agreement with the approximation of the signal cross section given in Ref. [21].

For comparison we show in Fig. 10 the acceptance integrated cross section depending on $m_{e^+e^-}$ for a proton target with a beam energy of $E_0 = 80$ MeV. In the left panel, the same curves as in Fig. 9 are plotted. In the right panel of Fig. 10, it is demonstrated that the VCS contribution corresponding with the Feynman diagrams in Fig. 2 are smaller by more than 6 orders of magnitude in the chosen kinematic setting and can thus be neglected. As indicated by the shape of the curves for $\Delta\sigma^{\mathrm{SL+TL}}_{\gamma^*,\mathrm{D+X}}$ and $\Delta\sigma^{\mathrm{TL}}_{\gamma^*,\mathrm{D}}$ in Figs. 9 and 10, the ratio of these two quantities is

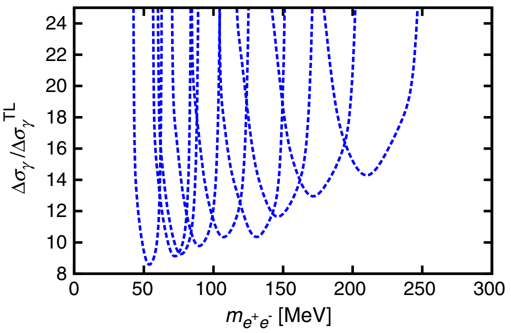

FIG. 8 (color online). Combined plot of our result for the ratios $\Delta\sigma_\gamma/\Delta\sigma_\gamma^{\mathrm{TL}}$ of each setting, starting with the lowest beam energy on the left.

TABLE II. Kinematics of the MAMI 2012 γ' search. Electron scattering angle: $\phi_- = 20.01°$ (spectrometer A). Positron scattering angle: $\phi_+ = -15.63°$ (spectrometer B). The number in the label of the kinematics refers to the invariant mass around which a setting is centered.

	E_0 [MeV]	$\lvert\vec{l}\rvert_+$ [MeV]	$\lvert\vec{l}\rvert_-$ [MeV]
kin057	180	78.7	98
kin072	240	103.6	132.0
kin077	255	110.1	140.4
kin091	300	129.5	164.5
kin109	360	155.4	197.6
kin138	435	190.7	247.7
kin150	495	213.7	271.6
kin177	585	250.0	317.3
kin218	720	309.2	392.7

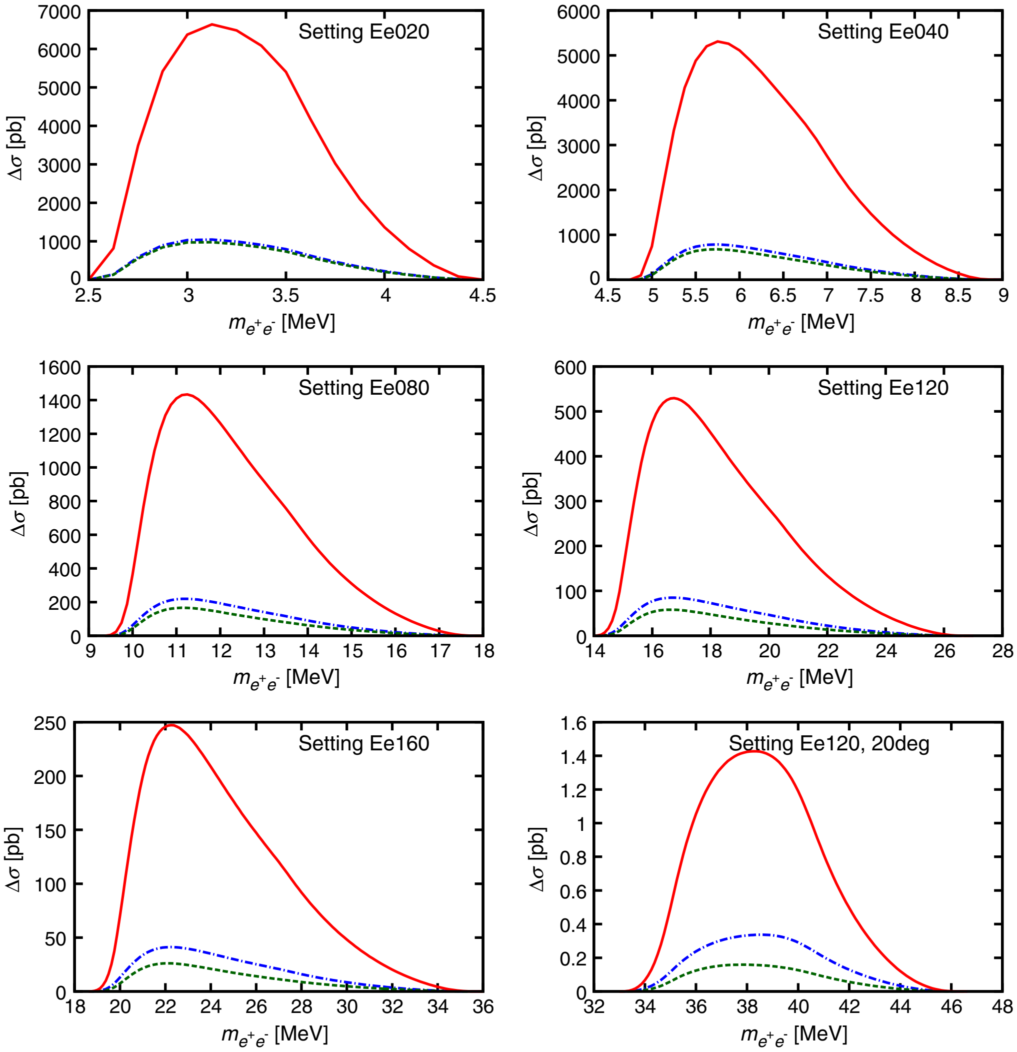

FIG. 9 (color online). Invariant mass distributions from the feasibility study for the MESA experiment. Solid curve: SL + TL (direct + exchange term), dashed curve: direct TL, dashed-dotted curve: direct SL + TL.

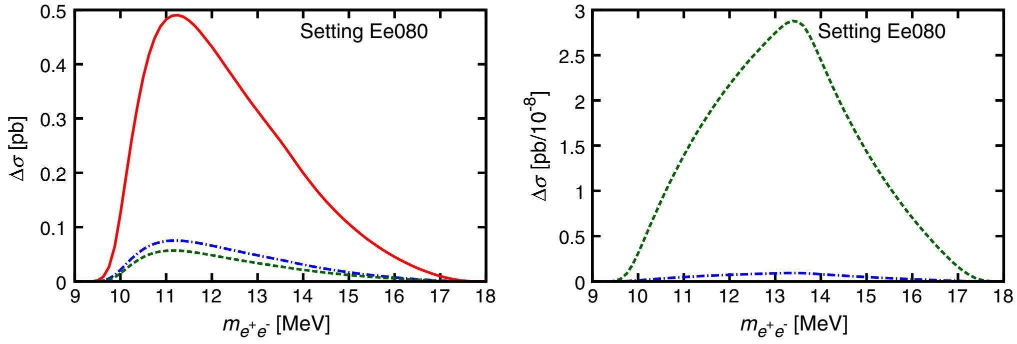

FIG. 10 (color online). Left panel: Invariant mass distributions from the feasibility study for the MESA experiment for a proton target. Solid curve: SL + TL (direct + exchange term), dashed curve: direct TL, dashed-dotted curve: direct SL + TL. Right panel: Isolated VCS cross section. Dashed curve: exchange term contribution, dashed-dotted curve: direct contribution.

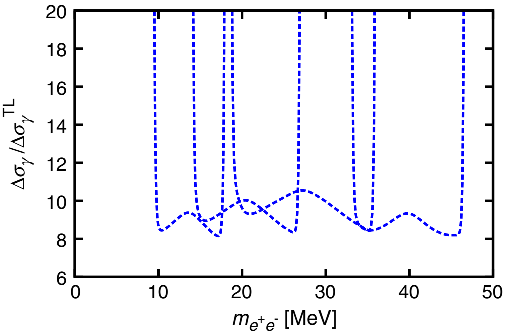

FIG. 11 (color online). Combined plot of our result for the ratio $\Delta\sigma_\gamma/\Delta\sigma_\gamma^{\rm TL}$ of each setting for the MESA experiment. The settings correspond with the following beam energies and scattering angles (from left to right): $E_0 = 80$, 120, 160 MeV with $\phi_\mp = \pm 10°$, $E_0 = 120$ MeV with $\phi_\mp = \pm 20°$.

equal, and thus the kind of target does not affect the exclusion limit concerning the QED background.

Figure 11 shows the calculated ratio $\Delta\sigma_\gamma/\Delta\sigma_\gamma^{\rm TL}$ which reaches a value around 8–10 for the proposed settings. The expected exclusion limit on ε^2 as obtained from Eq. (14), to the invariant mass spectra of Fig. 9, is presented in Fig. 12, where a mass resolution of 0.125 MeV was assumed. The dotted (dashed-dotted) curve in Fig. 12 represents the settings with a central angle of 10° (20°). At very low masses below 10 MeV Eq. (14) does not serve as a good approximation for the exclusion limit anymore since Eq. (19) of Ref. [21] overestimates the γ' signal cross section by up to 50%.

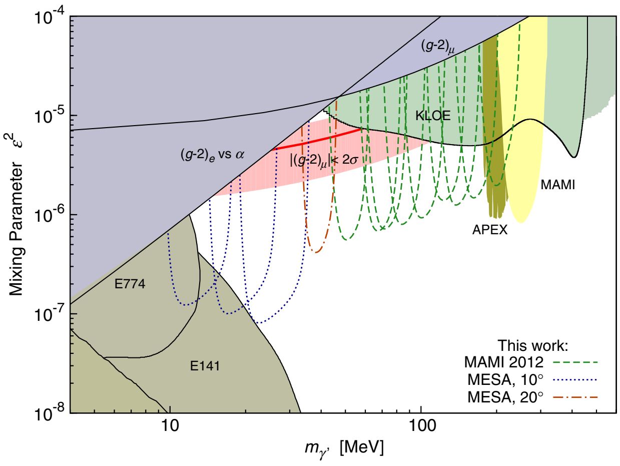

FIG. 12 (color online). Compilation of existing exclusion limits and our predictions: For a better visualization, we restrict ourselves to the region currently accessible at fixed-target experiments. Only existing limits as published in Refs. [16,21,36,37,40,41] are shown, represented by the shaded regions. We do not show the predictions for other experiments [26,28–30] in this figure which are scheduled to probe the same region of parameter space. The limits of MAMI and APEX are those as given in their publications [25,27]. The prediction of this work for the exclusion limit expected for the MAMI 2012 experiment discussed in Sec. III B is depicted by the dashed curves. The prediction for MESA obtained in Sec. IV is indicated by the dotted (dashed-dotted) curve for the setups with a central scattering angle of 10° (20°).

A compilation of the existing exclusion limits is presented in Fig. 12, which shows the region 5 MeV $\leq m_{\gamma'} \leq$ 600 MeV and $10^{-8} \leq \varepsilon^2 \leq 10^{-4}$ accessible at fixed-target experiments. Furthermore, existing limits as published in Refs. [16,21,36,37,40,41] are also shown and are represented by the shaded regions. Let us mention that other planned experiments [26,28–30] are scheduled to probe the same region of parameter space. The limits of MAMI and APEX are those as given in their publications [25,27]. Our prediction for the exclusion limit expected in the MAMI 2012 experiment discussed in Sec. III B is depicted by the dashed curves. The prediction for MESA obtained in Sec. IV is indicated by the dotted (dashed-dotted) curves for the setups with a central scattering angle of 10° (20°). Our calculation shows that the 2012 experiment is well suited to exclude a large region of the parameter space and in particular most of the so-called $(g-2)_\mu$ welcome band, in which the discrepancy between the experimental and theoretical value of the anomalous magnetic moment of the muon $(g-2)_\mu$ could be due to γ' contribution.

We propose an experiment for the MESA accelerator under construction at Mainz. The investigated kinematic settings will allow for the exclusion of the remaining part of the $(g-2)_\mu$ welcome band that is not probed so far.

V. CONCLUSIONS AND OUTLOOK

In this work we have calculated the cross sections which are crucial to describe the existing and planned fixed-target γ' search experiments. A comparison of our calculations with a sample of data taken at MAMI has been performed. After applying the leading-order QED radiative corrections for the corresponding elastic electron-hadron scattering process, we find that our calculations and the data sample are in good agreement. In addition, a calculation of the separated spacelike and timelike virtual photon exchange cross sections, each for the direct and exchange term, has been performed. This allows us to study the dependence of the background cross section on these contributions. Furthermore, we find that it is necessary to include the exchange term into the cross section in order to reconcile the data. The exchange contribution is contributing to the irreducible background.

Using the cross sections obtained in our analysis, we are able to provide predictions for the expected exclusion limits for MAMI and MESA. Following our predictions, the experiments at MAMI and MESA will be able to probe the entire $(g-2)_\mu$ welcome band and, in addition, increase the existing limits by 1 order of magnitude.

ACKNOWLEDGMENTS

This work was supported in part by the Research Centre “Elementarkräfte und Mathematische Grundlagen” at the Johannes Gutenberg University Mainz, the federal state of Rhineland-Palatinate, and in part by the Deutsche Forschungsgemeinschaft DFG through the Collaborative Research Center “The Low-Energy Frontier of the Standard Model” (SFB 1044) and the Cluster of Excellence “Precision Physics, Fundamental Interactions and Structure of Matter” (PRISMA). T. B. would like to thank Björn Walk for helpful discussions on GPU programming. Furthermore, we thank Achim Denig for useful discussions.

APPENDIX: DETAILED CROSS SECTION CALCULATIONS FOR γ' SEARCH EXPERIMENTS

Starting from Eq. (7), one finds by inserting $1 = \int d^4q'\delta^{(4)}(q' - l_+ - l_-)$

$$d\sigma = \frac{1}{4\sqrt{(k\cdot p)^2 - m^2M^2}} \frac{d^3\vec{k}'}{(2\pi)^3 2E'_e} \frac{d^3\vec{p}'}{(2\pi)^3 2E'_p} \frac{d^3\vec{q}'}{(2\pi)^3 2q'^0} (2\pi)^4\delta^{(4)}(k + p - k' - p' - q') \cdot \frac{d^3\vec{l}_-}{(2\pi)^3 2E_-} \frac{d^3\vec{l}_+}{(2\pi)^3 2E_+}$$
$$\cdot \underbrace{\frac{q'^0 dq'^0}{2\pi}}_{dq'^2/(2\pi)} (2\pi)^4\delta^{(4)}(q' - l_+ - l_-)\overline{|\mathcal{M}|^2}.$$

The δ functions constrain the three-momenta,

$$\vec{q} = \vec{l}_- + \vec{l}_+ \quad \text{and} \quad \vec{p}' = \vec{k} - \vec{k}' - \vec{q}',$$

which leads to

$$d\sigma = \frac{1}{128|\vec{k}|M} \frac{1}{(2\pi)^8} \frac{|\vec{k}'|^2|\vec{l}_+|^2|\vec{l}_-|^2}{E_{p'}E_{k'}E_{A'}E_{l_+}E_{l_-}} d|\vec{k}'|d\Omega_{e'}d|\vec{l}_+|d\Omega_+d|\vec{l}_-|d\Omega_-dq'^2 \underbrace{\delta(E_0 + M - E_{e'} - E_{p'} - q'^0)}_{=:\delta_1}$$
$$\times \underbrace{\delta(q'^0 - E_+ - E_-)}_{=:\delta_2}\overline{|\mathcal{M}|^2}. \tag{A1}$$

The remaining two delta functions can be used to express the energies associated with k' and l_-, by which integration over their three-momentum absolute values is performed. Therefore, expressions for $|\vec{k}'|$ and $|\vec{l}_-|$ in terms of the remaining quantities have to be found, using

$$q'^2 = 2m_l^2 + 2E_+E_- - 2|\vec{l}_-|\vec{l}_+ \cdot \hat{l}_- \Leftrightarrow 0 = \underbrace{\left(-\frac{q'^2}{2} + m_l^2\right)}_{=:A} + E_+E_- - |\vec{l}_-|\underbrace{\vec{l}_+ \cdot \hat{l}_-}_{=:B}. \tag{A2}$$

This equation can be rewritten as a quadratic equation for $|\vec{l}_-|$ which can be easily solved. After adding $(B|\vec{l}_-| - A)$ on both sides of Eq. (A2), squaring the result, and using $E_-^2 = |\vec{l}_-|^2 + m_l^2$, one finds the two solutions

$$|\vec{l}_-|_{1,2} = \frac{AB}{B^2 - E_+^2} \pm \sqrt{\frac{(AE_+)^2 + (E_+m_lB)^2 - (E_+^2m_l)^2}{(B^2 - E_+^2)^2}}. \tag{A3}$$

The determination of the physical solution can be done by considering the particles as massless. Now the calculation simplifies to

$$q'^2 = \underbrace{l_+^2 + l_-^2}_{=0} + 2|\vec{l}_-||\vec{l}_+|(1 - \hat{l}_+ \cdot \hat{l}_-) \Leftrightarrow |\vec{l}_-| = \frac{q'^2}{2|\vec{l}_+|(1 - \hat{l}_+ \cdot \hat{l}_-)}. \tag{A4}$$

Comparing Eqs. (A3) and (A4), one finds that the solution with "+" corresponds to the physical allowed case. Thus, it is

$$|\vec{l}_-| = \frac{AB}{B^2 - E_+^2} + \sqrt{\frac{(AE_+)^2 + (E_+ m_l B)^2 - (E_+^2 m_l)^2}{(B^2 - E_+^2)^2}}, \tag{A5}$$

with $A = -q'^2/2 + m^2$ and $B = \vec{l}_+ \cdot \hat{l}_-$.

The calculation of $|\vec{k}'|$ is done in a similar way. Since it is not necessary that the four-vectors l_+ and l_- appear explicitly in the following, instead their sum $q'^2 = (l_+ + l_-)^2$ is used where $|\vec{l}_-|$ is symbolic for the result of Eq. (A5). Again starting from four-momentum conservation, one finds

$$\Leftrightarrow 0 = \underbrace{(p + k - q')^2 + m^2 - M^2}_{=:D} \underbrace{- \, 2(E_0 + M - q'^0)}_{=:F} E_{e'} + \underbrace{2(\vec{k} - \vec{q}') \cdot \hat{k}'}_{=:G} |\vec{k}'|.$$

An analogous calculation as for $|\vec{l}_-|$ then leads to

$$|\vec{k}'| = -\frac{DG}{G^2 - F^2} + \sqrt{\frac{(mFG)^2 + (DF)^2 - (mF^2)^2}{(G^2 - F^2)^2}}. \tag{A6}$$

Thus, one has

$$\frac{\partial \delta_1}{\partial |\vec{k}'|} = \frac{\partial}{\partial |\vec{k}'|}(E_0 + M - E_{e'} - E_{p'} - q'^0) = -\frac{|\vec{k}'|}{E_{k'}} - \frac{|\vec{k}'| - \hat{k}' \cdot (\vec{k} - \vec{q}')}{E_{p'}} \tag{A7}$$

and

$$\frac{\partial \delta_2}{\partial |\vec{l}_-|} = \frac{\partial}{\partial |\vec{l}_-|}(q'^0 - E_+ - E_-) = -\frac{|\vec{l}_-|}{E_-} + \frac{|\vec{l}_-| + \vec{l}_+ \cdot \hat{l}_-}{q'^0}. \tag{A8}$$

For the experiments performed at MAMI, the detector quantities are given in Table I. The horizontal and vertical acceptances are given in a Cartesian reference frame. It is convenient to calculate the cross section directly in the lab frame. The lab frame three-momenta of the detected particles depending on these quantities are parametrized by

$$\vec{l}_\pm = \frac{|\vec{l}_\pm|}{\sqrt{1 + \tan^2\delta\theta + \tan^2\delta\phi}} \begin{pmatrix} \tan\delta\phi\cos\phi_0 + \sin\phi_0 \\ \tan\delta\theta \\ \cos\phi_0 - \tan\delta\phi\sin\phi_0 \end{pmatrix},$$

where ϕ_0 is the central horizontal angle of the detector, $\delta\phi$ is the deviation from the horizontal scattering angle, and $\delta\theta$ is the deviation from the vertical out-of-plane angle. Note that the vertical central angle of the detectors is 0°. Integrating over the angles $\delta\phi$ and $\delta\theta$ within the limits of the experimental acceptances then leads to the cross section $\Delta\sigma$. To account for this geometry, the cross section has to be multiplied by a Jacobian,

$$J(\delta\phi, \delta\theta) = \left| \frac{1}{\cos^2\delta\phi\cos^2\delta\theta(1 + \tan^2\delta\theta + \tan^2\delta\phi)^{3/2}} \right|.$$

The cross section then reads

$$\frac{d\sigma}{d|\vec{l}_+| d\Omega_+ d\Omega_- d\Omega_{e'} dq'^2} = \frac{1}{128|\vec{k}|M} \frac{1}{(2\pi)^8} \frac{|\vec{k}'|^2 |\vec{l}_+|^2 |\vec{l}_-|^2}{E_{p'} E_{k'} E_{A'} E_+ E_-} J(\delta\phi_-, \delta\theta_-) J(\delta\phi_+, \delta\theta_+) \left(\left| \frac{\partial \delta_1}{\partial |\vec{k}'|} \right| \left| \frac{\partial \delta_2}{\partial |\vec{l}_-|} \right| \right)^{-1} \overline{|\mathcal{M}|^2}. \tag{A9}$$

---

[1] G. Aad *et al.* (ATLAS Collaboration), Phys. Lett. B **716**, 1 (2012).

[2] S. Chatrchyan *et al.* (CMS Collaboration), Phys. Lett. B **716**, 30 (2012).

[3] J. Beringer *et al.* (Particle Data Group Collaboration), Phys. Rev. D **86**, 010001 (2012).

[4] G. Bertone, D. Hooper, and J. Silk, Phys. Rep. **405**, 279 (2005).

[5] N. Jarosik *et al.*, Astrophys. J. Suppl. Ser. **192**, 14 (2011); D. Larson *et al.*, Astrophys. J. Suppl. Ser. **192**, 16 (2011); E. Komatsu *et al.* (WMAP Collaboration), Astrophys. J. Suppl. Ser. **192**, 18 (2011).

[6] A. W. Strong, R. Diehl, H. Halloin, V. Schönfelder, L. Bouchet, P. Mandrou, F. Lebrun, and R. Terrier, Astron. Astrophys. **444**, 495 (2005).

[7] O. Adriani *et al.* (PAMELA Collaboration), Nature (London) **458**, 607 (2009).

[8] I. Cholis, G. Dobler, D. P. Finkbeiner, L. Goodenough, and N. Weiner, Phys. Rev. D **80**, 123518 (2009).

[9] N. Arkani-Hamed, D. P. Finkbeiner, T. R. Slatyer, and N. Weiner, Phys. Rev. D **79**, 015014 (2009).

[10] M. Pospelov and A. Ritz, Phys. Lett. B **671**, 391 (2009).

[11] S. Weinberg, Phys. Rev. Lett. **40**, 223 (1978).

[12] L. B. Okun, Sov. Phys. JETP **56**, 502 (1982).

[13] B. Holdom, Phys. Lett. B **178**, 65 (1986).

[14] P. Fayet, Nucl. Phys. **B347**, 743 (1990).

[15] M. Pospelov, Phys. Rev. D **80**, 095002 (2009).

[16] S. Andreas, M. D. Goodsell, and A. Ringwald, Phys. Rev. D **87**, 025007 (2013).

[17] P. Fayet, Phys. Rev. D **75**, 115017 (2007).

[18] C. Cheung, J. T. Ruderman, L.-T. Wang, and I. Yavin, Phys. Rev. D **80**, 035008 (2009).

[19] R. Essig, P. Schuster, and N. Toro, Phys. Rev. D **80**, 015003 (2009).

[20] M. Goodsell, J. Jaeckel, J. Redondo, and A. Ringwald, J. High Energy Phys. 11 (2009) 027.

[21] J. D. Bjorken, R. Essig, P. Schuster, and N. Toro, Phys. Rev. D **80**, 075018 (2009).

[22] B. Batell, M. Pospelov, and A. Ritz, Phys. Rev. D **79**, 115008 (2009).

[23] M. Reece and L.-T. Wang, J. High Energy Phys. 07 (2009) 051.

[24] B. Batell, M. Pospelov, and A. Ritz, Phys. Rev. D **80**, 095024 (2009).

[25] H. Merkel *et al.* (A1 Collaboration), Phys. Rev. Lett. **106**, 251802 (2011).

[26] R. Essig, P. Schuster, N. Toro, and B. Wojtsekhowski, J. High Energy Phys. 02 (2011) 009.

[27] S. Abrahamyan *et al.* (APEX Collaboration), Phys. Rev. Lett. **107**, 191804 (2011).

[28] The Heavy Photon Search Collaboration (HPS), https://confluence.slac.stanford.edu/display/hpsg/.

[29] M. Freytsis, G. Ovanesyan, and J. Thaler, J. High Energy Phys. 01 (2010) 111.

[30] Y. Kahn and J. Thaler, Phys. Rev. D **86**, 115012 (2012).

[31] J. Blumlein and J. Brunner, Phys. Lett. B **701**, 155 (2011).

[32] S. N. Gninenko, Phys. Rev. D **85**, 055027 (2012).

[33] S. N. Gninenko, Phys. Lett. B **713**, 244 (2012).

[34] S. Andreas, C. Niebuhr, and A. Ringwald, Phys. Rev. D **86**, 095019 (2012).

[35] B. Aubert *et al.* (*BABAR* Collaboration), Phys. Rev. Lett. **103**, 081803 (2009).

[36] F. Archilli *et al.*, Phys. Lett. B **706**, 251 (2012).

[37] D. Babusci *et al.* (KLOE-2 Collaboration), Phys. Lett. B **720**, 111 (2013).

[38] B. Echenard, Mod. Phys. Lett. A **27**, 1230016 (2012).

[39] S. N. Gninenko, Phys. Rev. D **87**, 035030 (2013).

[40] H. Davoudiasl, H.-S. Lee, and W. J. Marciano, Phys. Rev. D **86**, 095009 (2012).

[41] M. Endo, K. Hamaguchi, and G. Mishima, Phys. Rev. D **86**, 095029 (2012).

[42] J. L. Hewett *et al.*, arXiv:1205.2671.

[43] J. D. Bjorken and S. D. Drell, *Relativistic Quantum Mechanics* (McGraw-Hill, New York, 1964).

[44] J. Friedrich and N. Voegler, Nucl. Phys. **A373**, 192 (1982).

[45] M. Vanderhaeghen, J. Friedrich, D. Lhuillier, D. Marchand, L. Van Hoorebeke, and J. Van de Wiele, Phys. Rev. C **62**, 025501 (2000).

[46] G. P. Lepage, J. Comput. Phys. **27**, 192 (1978).

[47] CUDA web page, https://developer.nvidia.com/cuda-toolkit.

[48] J. Kanzaki, Eur. Phys. J. C **71**, 1559 (2011).

[49] K. I. Blomqvist *et al.*, Nucl. Instrum. Methods Phys. Res., Sect. A **403**, 263 (1998).

Search at the Mainz Microtron for Light Massive Gauge Bosons Relevant for the Muon $g-2$ Anomaly

H. Merkel,[1,*] P. Achenbach,[1] C. Ayerbe Gayoso,[1,†] T. Beranek,[1] J. Beričič,[2] J. C. Bernauer,[1,‡] R. Böhm,[1] D. Bosnar,[3] L. Correa,[1] L. Debenjak,[2] A. Denig,[1] M. O. Distler,[1] A. Esser,[1] H. Fonvieille,[4] I. Friščić,[3] M. Gómez Rodríguez de la Paz,[1] M. Hoek,[1] S. Kegel,[1] Y. Kohl,[1] D. G. Middleton,[1] M. Mihovilovič,[1] U. Müller,[1] L. Nungesser,[1] J. Pochodzalla,[1] M. Rohrbeck,[1] G. Ron,[5] S. Sánchez Majos,[1] B. S. Schlimme,[1] M. Schoth,[1] F. Schulz,[1] C. Sfienti,[1] S. Širca,[2,6] M. Thiel,[1] A. Tyukin,[1] A. Weber,[1] and M. Weinriefer[1]
(A1 Collaboration)

[1]*Institut für Kernphysik, Johannes Gutenberg-Universität Mainz, D-55099 Mainz, Germany*
[2]*Jožef Stefan Institute, SI-1000 Ljubljana, Slovenia*
[3]*Department of Physics, University of Zagreb, HR-10002 Zagreb, Croatia*
[4]*Clermont Université, Université Blaise Pascal, CNRS/IN2P3, LPC, BP 10448, F-63000 Clermont-Ferrand, France*
[5]*Racah Institute of Physics, Hebrew University of Jerusalem, Jerusalem 91904, Israel*
[6]*Department of Physics, University of Ljubljana, SI-1000 Ljubljana, Slovenia*

(Received 22 April 2014; revised manuscript received 19 May 2014; published 4 June 2014)

A massive, but light, Abelian $U(1)$ gauge boson is a well-motivated possible signature of physics beyond the standard model of particle physics. In this Letter, the search for the signal of such a $U(1)$ gauge boson in electron-positron pair production at the spectrometer setup of the A1 Collaboration at the Mainz Microtron is described. Exclusion limits in the mass range of 40 MeV/c^2 to 300 MeV/c^2, with a sensitivity in the squared mixing parameter of as little as $\epsilon^2 = 8\times10^{-7}$ are presented. A large fraction of the parameter space has been excluded where the discrepancy of the measured anomalous magnetic moment of the muon with theory might be explained by an additional $U(1)$ gauge boson.

DOI: 10.1103/PhysRevLett.112.221802 PACS numbers: 14.70.Pw, 13.40.Em, 25.30.Rw, 95.35.+d

Introduction.—The completion of the standard model (SM) of particle physics by the discovery of the Higgs particle at the Large Hadron Collider (LHC) is undoubtedly a remarkable success after decades of particle physics experiments [1]. This success, however, also emphasizes one of the major unresolved questions of today's physics: The existence of dark matter in the Universe, which has been meanwhile well established, is one of the most pressing indications of the need for new physics beyond the SM. Because there have yet been no experimental hints from the LHC for supersymmetry, which has for decades provided the most promising candidate for dark matter from particle physics, the search for physics beyond the SM must be extended to more general concepts.

Given the rich structure of the SM, it would not be surprising to have a similar rich structure for a possible "dark sector," consisting of particles and interactions that have only a tiny interaction with SM matter and fields. Most extensions of the SM, e.g., string theory, provide such a rich structure, which has to be broken down to the observed SM.

In recent years, a particularly well-motivated portal to such a dark sector, the search for a massive $U(1)$ gauge boson [2], triggered a vast amount of theoretical and experimental activities. Such a $U(1)$ gauge boson, sometimes called "dark photon" or γ', arises naturally in several extensions of the SM as the lowest-rank interaction of this sector (see, e.g., Refs. [3–5] for an overview).

The residual interaction of a dark photon with SM matter is given in the simplest model by kinematic mixing [6,7], producing an effective interaction $\epsilon e A'_\mu J^\mu$ of the dark-photon field A' with the electric current J. The strength of this interaction is given by the mixing parameter $\epsilon = \sqrt{\alpha'/\alpha}$, equal to the square root of the ratio of dark and SM electromagnetic couplings, which is not required to be small from first principles. Assuming that ϵ vanishes at high energies, ϵ can be generated by perturbative corrections, including particles which are charged both under electromagnetic interaction and the $U(1)$ interaction, leading to a natural scale of $\epsilon \sim 10^{-8} - 10^{-2}$. Including nonperturbative models, values of $\epsilon \sim 10^{-12} - 10^{-3}$ have been discussed [8,9].

In addition to the strong motivation from models and theory, several experimental phenomena could be explained by such a dark photon. A dark sector with an annihilation channel to dark photons could explain, e.g., the positron excess in the Universe measured first by PAMELA [10] and later confirmed by the Fermi LAT Collaboration [11] and AMS-02 [12]. While other positron sources, for example quasars, are also discussed in the literature, the dark-photon annihilation process provides a good fit to the positron spectrum.

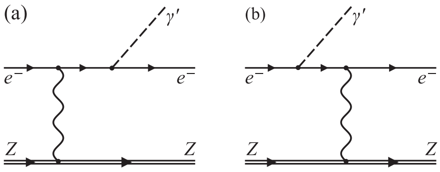

FIG. 1. Radiative production of a γ' in final (a) and initial (b) state on a heavy target nucleus Z. The subsequent decay of the γ' to an electron-positron pair would be the unique signal of such a γ' with a sharp mass distribution.

Of special interest for the parameter range probed in this experiment is the discrepancy of the measured anomalous magnetic moment $(g-2)$ of the muon [13] in comparison with SM calculations [14]. This discrepancy could be explained by loop contributions of dark photons with a mass range of 10–200 MeV$/c^2$ and a mixing parameter squared around $\epsilon^2 \approx 10^{-5}$ [15,16].

This Letter describes the search for a dark photon in the mass region of 40–300 MeV$/c^2$ by a fixed-target electron scattering experiment. A possible dark photon could be produced radiatively on a heavy target nucleus with high Z (see Fig. 1), followed by a subsequent decay into an electron-positron pair [17]. Since this decay is suppressed by the small squared mixing parameter ϵ^2, the decay width would be far below the experimental resolution, resulting in a sharp peak in the invariant mass of the produced lepton pair.

This peak is expected to be on top of a smooth background of standard radiative electron-positron pair production via a virtual photon. This background can be calculated in QED; the tools to integrate the background and a possible signal over the acceptance of the experiment were developed and discussed in detail in Refs. [18,19].

Experiment.—The experiment was performed at the spectrometer setup of the A1 Collaboration at the Mainz Microtron (see Ref. [20] for a detailed description). The experimental technique was similar to the technique used in the precursor experiment [21], with a few modifications of the target and of the vacuum system to further reduce multiple scattering and to improve the overall mass resolution.

Table I summarizes the kinematical settings. For all settings, the incoming electron beam of the accelerator hits a target consisting of one or several strips of tantalum foils (99.99% ^{181}Ta); the thickness of each separate foil is between 1 and 6 μm. For each setting, the target configuration was separately optimized for maximum luminosity, with minimized load by radiation background in the focal plane detectors of the spectrometers.

For the detection of the lepton pair from the decay of a possible dark photon, the spectrometers A and B of the A1 setup were placed at their minimal angle (see Table I). With these fixed angles, the settings were adjusted to cover the production of a dark photon in the beam direction and to cover the maximum energy transfer to the dark photon. The choice of the polarity of the spectrometers was given by the background conditions. Since the theoretical description of the background process improved during the analysis, it

TABLE I. Kinematical settings. All settings were centered around the production of lepton pairs in the beam direction and with maximum energy transferred to the pair.

Setting	Central mass (MeV$/c^2$)	Beam energy E_0 (MeV)	θ_{e+}	p_{e+} (MeV$/c$)	θ_{e-}	p_{e-} (MeV$/c$)	e^+ in spectrometer	e^- in spectrometer	Collimator A (msr)	Collimator B (msr)	Target
1	54	180	20.0°	74.0	15.1°	97.1	A	B	28	5.6	single foil
2	54	180	15.1°	100.3	20.0°	74.0	B	A	21	5.6	single foil
3	57	180	20.0°	78.7	15.6°	98.0	A	B	21	5.6	single foil
4	72	240	20.0°	103.6	15.6°	132.0	A	B	21	5.6	single foil
5	76	255	20.0°	105.0	15.1°	137.3	A	B	28	5.6	single foil
6	77	255	20.0°	110.1	15.6°	140.4	A	B	21	5.6	single foil
7	91	300	20.0°	129.5	15.6°	164.6	A	B	21	5.6	single foil
8	103	345	20.0°	142.0	15.1°	186.5	A	B	28	5.6	foil stack
9	109	360	20.0°	155.4	15.6°	197.6	A	B	21	5.6	single foil
10	135	450	20.0°	185.0	15.1°	243.3	A	B	28	5.6	foil stack
11	138	435	15.6°	244.0	20.0°	190.7	B	A	21	5.6	single foil
12	138	435	15.6°	233.9	20.0°	190.0	B	A	21	5.6	single foil
13	138	435	20.0°	190.0	15.6°	244.5	A	B	21	5.6	single foil
14	138	435	20.0°	190.0	15.6°	234.1	A	B	21	5.6	single foil
15	150	495	20.0°	213.7	15.6°	271.1	A	B	21	5.6	foil stack
16	170	570	20.0°	234.0	15.1°	307.3	A	B	28	5.6	foil stack
17	177	585	20.0°	250.0	15.6°	317.3	A	B	21	5.6	foil stack
18	202	675	15.1°	367.0	20.0°	277.2	B	A	21	5.6	single foil
19	218	720	20.0°	309.2	15.6°	392.7	A	B	21	5.6	foil stack
20	256	855	20.0°	351.0	15.1°	460.3	A	B	28	5.6	foil stack
21	270	855	15.2°	509.4	22.8°	346.3	B	A	21	5.6	single foil
22	270	855	15.1°	511.7	20.0°	346.3	B	A	21	5.6	single foil

turns out that some of these settings were not chosen optimally. The settings of the pilot experiment [21] were included, and were reanalyzed with additional event samples covering the same mass region.

The vacuum system of the spectrometers was connected to the scattering chamber to minimize multiple scattering. Both spectrometers were equipped with four layers of vertical drift chambers for position resolution, two layers of scintillator detectors for trigger and timing purposes, and gas Čerenkov detectors for pion-electron separation and further background reduction.

The beam current of up to $I = 80\ \mu$A was measured with a flux-gate magnetometer (Förster probe). The angular acceptances of the spectrometers were defined by heavy metal collimators. For spectrometer B, a collimator setting of 40 mrad (horizontal) $\times$ 140 mrad (vertical) $= 5.6$ msr was used for all settings, while for spectrometer A two different collimators with 150×140 mrad $= 21$ msr and 200×140 mrad $= 28$ msr were used. The momentum acceptance of the spectrometers was 20% for spectrometer A and 15% for spectrometer B.

Data analysis.—The lepton pair was detected in coincidence between the two spectrometers. For reaction identification, a cut was applied first on a signal in the Čerenkov detectors of both spectrometers with an efficiency of $\approx 98\%$. The coincidence time between spectrometer A and B was corrected for the path length in spectrometer A of ≈ 10 m and spectrometer B of ≈ 12 m. After this correction, a clear coincidence peak with a width of less than 1 ns (FWHM) was seen. The range of $|\Delta t_{AB}| < 1$ ns was used to identify lepton pairs. The background contribution from random coincidences was estimated by a cut on the sideband with $5\ \text{ns} < |\Delta t_{AB}| < 15$ ns.

Additional cuts were applied for the acceptance of the spectrometers to further reduce the contribution of backscattered particles from the entrance flange of spectrometer B. Finally, cuts on the validity of the overall kinematics were applied to remove, e.g., accidental coincidences where the total energy of the pair exceeds the beam energy.

In total, the background contribution ranges from 4% up to 11% after all cuts. This background contribution is not subtracted for the peak search, but has to be taken into account later in the calculation of the exclusion limit.

For the identified lepton pairs, the invariant pair mass was determined by the four-momenta of the leptons via $m^2_{e+e-} = (p_{e^+} + p_{e^-})^2$. Figure 2 shows the mass distribution of all settings.

To add up the pair mass distribution of all settings, the absolute mass calibration of each setting has to be better than the expected peak width. The magnetic field of the spectrometers was simultaneously monitored with NMR probes to $\delta B/B = 10^{-4}$ and with Hall probes on the $\delta B/B = 5 \times 10^{-4}$ level. This translates, in total, to a mass calibration of better than 100 keV$/c^2$. The calibration was verified at several points by additional measurements of elastic scattering on tantalum. The position and width of the ^{181}Ta ground state was used to confirm the total calibration and to extract the momentum and angular resolution of the total setup *in situ*. The experimental resolutions were used to tune the detailed simulation of the elastic scattering process to reproduce the elastic peak shape. Finally, the simulation was used to determine the mass resolution and expected dark-photon peak shape, which depend on the mass including radiative corrections. The resulting resolution varies between 210 keV$/c^2$ FWHM, in the lowest mass range, up to 920 keV$/c^2$ FWHM, for the settings of the last experiment.

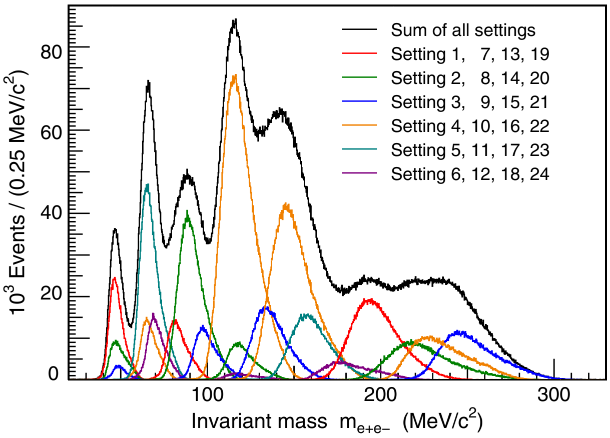

FIG. 2 (color online). Mass distribution of the individual settings (color or shaded) and of the sum (black). The experiment probes the invariant mass region between 40 and 300 MeV$/c^2$.

The estimated peak shape was used to perform a search for a peak in the total mass distribution. For this, the background for each bin was estimated by a local fit of the neighboring bins with a cubic polynomial. The confidence interval was determined using the Feldman-Cousins algorithm [22]. (Please note that in the literature several different approaches were used by different experiments to determine limits for dark-photon searches; however, they differ only by a few percent.) The results were corrected for the leakage of the peak outside the bin. The complete procedure was repeated with shifted binning limits in eight steps.

No significant signal for a dark photon was detected.

Results and interpretation.—Because of the use of thin tantalum foil stacks as targets, the normalization of the cross section contains large uncertainties. However, the identification of the QED background process is very clean, and can be used as normalization. Therefore, to translate the exclusion limit in terms of events to an exclusion limit in terms of the mixing parameter ϵ, we used the ratio of dark-photon production with mixing parameter ϵ divided by the QED background process [17],

$$R = \frac{d\sigma(X \to \gamma' Y \to e^+e^- Y)}{d\sigma(X \to \gamma^* Y \to e^+e^- Y)} = \frac{3\pi}{2N_f}\frac{\epsilon^2}{\alpha}\frac{m_{\gamma'}}{\delta_m}.$$

TABLE II. Systematic uncertainties.

Source	Uncertainty (%)
Calibration of the missing mass determination	0.1
Simulation of the expected peak shape	0.3
Fit of the background shape	0.2
Background subtraction	0.05
Normalization	2
Total (linear sum)	2.7

Here N_f is the ratio of the phase space of the decay into an e^+e^- pair to the phase space of the total decay (equal to 1 below $2m_\mu$), and δ_m is the bin width in mass. Please note that this particular choice of N_f implies that the dark photon decays only into SM matter. Exclusion limits for more general models, with invisible decays into light dark-sector particles with mass $m_X < m_{\gamma'}/2$, can be derived by scaling ϵ^2 with the corresponding branching ratio. For the virtual photon channel we used the background-subtracted mass distribution. To determine the ratio R, both cross sections as calculated in Ref. [18] were integrated over the acceptance of the experiment by standard Monte Carlo methods. Here, the normalization was chosen to reproduce the measured mass distribution.

Please note that in the interpretation of the data in Ref. [21], the cross sections were calculated not including the full antisymmetrization as discussed in Ref. [18]; this leads to an overestimation of the sensitivity by a factor of 2–3. Therefore, these data were included in this analysis and were reanalyzed. Because additional data were taken in the same mass range, roughly the same sensitivity was achieved.

Table II summarizes the systematic uncertainties of the measurement, including the systematic error of the interpretation as a limit in ϵ^2. The contribution of the missing mass calibration was estimated to be 0.1% by varying momentum and angular calibration in the simulation. The quality of the peak shape description via simulation was estimated, by the description of the peak shape of the elastic calibration settings, to contribute less than 2% in the shape itself, leading to an error in the leakage between the bins of 0.3%. The fit of the background by using neighboring bins introduces an additional statistical error from these bins; this is larger than the error in the shape and contributes 0.2% to the systematic error. The subtraction of the background of up to 11% is only used for the normalization and contributes 0.05% to the systematic error. The dominant systematic error originates from the normalization of the total yield, because the mass distribution of the QED calculation differs locally up to 2% from the measured distribution.

Figure 3 shows the resulting 2σ exclusion limits. Also included in the figure are the limits by the APEX [23], WASA-at-COSY [24], KLOE-2 [25], HADES [26], and *BABAR* [27,28] Collaborations. The red line shows the interpretation of the $a_\mu = (g-2)_\mu$ discrepancy as a dark photon with a 2σ error band (dashed lines) and as an exclusion limit (blue shaded region). Also included is the reanalysis of Ref. [29] of the beam dump experiment E774 [30] to extract exclusion limits for dark photons.

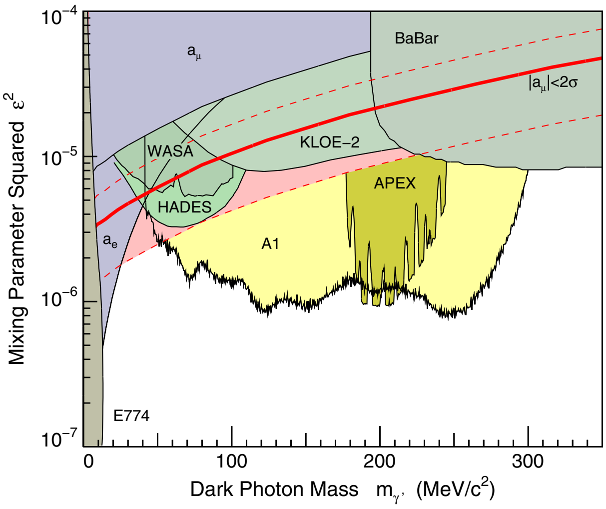

FIG. 3 (color online). Exclusion limits in terms of squared mixing parameter ϵ^2. The yellow (light shaded) area marked with A1 is excluded by this experiment.

With the new measurement presented here, the exclusion limit in the region of the $(g-2)$ anomaly of the muon was improved considerably. While the results of the meson decays by KLOE-2, WASA-at-COSY, and HADES were not able to completely rule out the dark photon as the origin of the anomaly, the new data set clearly covers the possible signal of the anomaly by several sigmas over a large mass range. The remaining undecided mass range of $25\ \mathrm{MeV}/c^2 \lesssim m_{\gamma'} \lesssim 50\ \mathrm{MeV}/c^2$ cannot be covered by the spectrometers of the A1 collaboration without modifications. However, several experiments by different collaborations are already planned to access the low mass region in the near future (see Ref. [19] for a summary).

The authors would like to thank the MAMI accelerator group for the excellent beam quality that made this experiment possible. This work was supported by the Collaborative Research Center 1044 and the State of Rhineland-Palatinate.

---

[*] merkel@kph.uni-mainz.de

[†] Present address: The College of William & Mary, Williamsburg, VA 23185, USA.

[‡] Present address: MIT-LNS, Cambridge, MA 02139, USA.

[1] S. Chatrchyan *et al.*, Phys. Lett. B **716**, 30 (2012).
[2] P. Fayet, Nucl. Phys. **B347**, 743 (1990).
[3] P. Langacker, Rev. Mod. Phys. **81**, 1199 (2009).
[4] P. Fayet, Phys. Rev. D **81**, 054025 (2010).

[5] J. Beringer *et al.* (Particle Data Group), Phys. Rev. D **86**, 010001 (2012).
[6] B. Holdom, Phys. Lett. **166B**, 196 (1986).
[7] P. Galison and A. Manohar, Phys. Lett. **136B**, 279 (1984).
[8] N. Arkani-Hamed and N. Weiner, J. High Energy Phys. 12 (2008) 104.
[9] R. Essig, P. Schuster, and N. Toro, Phys. Rev. D **80**, 015003 (2009).
[10] O. Adriani *et al.*, Nature (London) **458**, 607 (2009).
[11] M. Ackermann *et al.* (Fermi LAT Collaboration), Phys. Rev. Lett. **108**, 011103 (2012).
[12] M. Aguilar *et al.* (AMS Collaboration), Phys. Rev. Lett. **110**, 141102 (2013).
[13] G. W. Bennett *et al.*, Phys. Rev. D **73**, 072003 (2006).
[14] M. Davier, A. Hoecker, B. Malaescu, and Z. Zhang, Eur. Phys. J. C **71**, 1515 (2011).
[15] P. Fayet, Phys. Rev. D **75**, 115017 (2007).
[16] M. Pospelov, Phys. Rev. D **80**, 095002 (2009).
[17] J. D. Bjorken, R. Essig, P. Schuster, and N. Toro, Phys. Rev. D **80**, 075018 (2009).
[18] T. Beranek, H. Merkel, and M. Vanderhaeghen, Phys. Rev. D **88**, 015032 (2013).
[19] T. Beranek and M. Vanderhaeghen, Phys. Rev. D **89**, 055006 (2014).
[20] K. I. Blomqvist *et al.*, Nucl. Instrum. Methods Phys. Res., Sect. A **403**, 263 (1998).
[21] H. Merkel *et al.* (A1 Collaboration), Phys. Rev. Lett. **106**, 251802 (2011).
[22] G. J. Feldman and R. D. Cousins, Phys. Rev. D **57**, 3873 (1998).
[23] S. Abrahamyan *et al.* (APEX Collaboration), Phys. Rev. Lett. **107**, 191804 (2011).
[24] P. Adlarson *et al.* (WASA-at-COSY Collaboration), Phys. Lett. B **726**, 187 (2013).
[25] D. Babusci *et al.* (KLOE-2 Collaboration), Phys. Lett. B **720**, 111 (2013).
[26] G. Agakishiev *et al.* (HADES Collaboration), Phys. Lett. B **731**, 265 (2014).
[27] B. Aubert *et al.*, Phys. Rev. Lett. **103**, 081803 (2009).
[28] B. Echenard, Adv. High Energy Phys. **2012**, 514014 (2012).
[29] S. Andreas, C. Niebuhr, and A. Ringwald, Phys. Rev. D **86**, 095019 (2012).
[30] A. Bross, M. Crisler, S. Pordes, J. Volk, S. Errede, and J. Wrbanek, Phys. Rev. Lett. **67**, 2942 (1991).